Neutron-superfluid vortices and proton-superconductor flux tubes: Development of a minimal model for pulsar glitches

Sanjay Shukla,[1,*] Marc E. Brachet,[2,†] and Rahul Pandit[1,‡]

[1]*Centre for Condensed Matter Theory, Department of Physics, Indian Institute of Science,*
Bangalore 560012, India
[2]*Laboratoire de Physique de l'École Normale Supérieure, ENS, Université PSL,*
CNRS, Sorbonne Université, Université de Paris, 24 Rue Lhomond, 75005 Paris, France

(Received 21 May 2024; accepted 9 September 2024; published 1 October 2024)

We develop a theoretical framework that allows us to explore the coupled motion of neutron-superfluid vortices and proton-superconductor flux tubes in a gravitationally collapsed condensate, which describe neutron stars that form pulsars. Our framework uses the 3D Gross-Pitaevskii-Poisson-equation for neutron Cooper pairs, the real-time-Ginzburg-Landau equation for proton Cooper pairs, the Maxwell equations for the vector potential $\mathbf{A}$, and Newtonian gravity and interactions, both direct and induced by the Poisson equation, between the neutron and proton subsystems. For a pulsar we include a crust potential, characterized by an angle θ, and frictional drag. By carrying out extensive direct numerical simulations of this model, we obtain a variety of interesting results. We show that a rotating proton superconductor generates a uniform London magnetic field and the field distribution around flux tubes changes. In the absence of any direct interaction between the two species, they interact through the gravitational Poisson equation. The inclusion of the current-current interaction and the complete Maxwell equations allows us to quantify the entrainment effect that leads to induced magnetization of neutron vortices. We demonstrate that, with a strong external magnetic field $\mathbf{B}_{\mathrm{ext}}$, proton flux tubes are anchored to the crust, whereas neutron vortices leave the condensate and lead to abrupt changes of the crust angular momentum J_c. The frictional term in the dynamical equation for θ yields stick-slip dynamics that leads, in turn, to glitches in the time series of J_c. By calculating various statistical properties of this time series, we demonstrate that they display self-organized criticality that has been found in observations for several pulsars. We compare our results with those of earlier explorations of pulsar-glitch statistics in Gross-Pitaevskii equation-based minimal models for pulsars.

DOI: 10.1103/PhysRevD.110.083002

I. INTRODUCTION

Recent advances in the Gross-Pitaevskii-Poisson (GPP) modeling of bosonic [1] and axionic [2] stars have led to an elegant, minimal model for pulsars [3], which includes a crust potential, and leads naturally to pulsar glitches [4–6]. These GPP models have, so far, accounted only for bosons, e.g., the neutron superfluid in a neutron star [7]. Within the outer core of a neutron star, characterized by a density ranging from $\rho \simeq 5\times10^{13}\ \mathrm{g\,cm^{-3}}$ to $10^{15}\ \mathrm{g\,cm^{-3}}$ [7], lies a region consisting predominantly of neutrons (95% of the total mass) and some protons (5% of the total mass), and sufficient electrons to maintain charge neutrality; this region exhibits extraordinary properties; the neutron Cooper pairs form a superfluid [8] and the proton Cooper pairs a superconductor [7,9]. Pulsars are rapidly rotating and highly magnetized neutron stars [10,11] with magnetic fields $\simeq 10^{12}$ G. Our goal is to generalize the GPP modeling framework for pulsars [3] to include protons, which are in a superconducting state that is affected strongly by the magnetic field.

Neutrons in a neutron-star interiors are in a superfluid state, so when the star rotates with a sufficiently large angular velocity, quantized vortices are formed; each vortex has an angular momentum that is an integer multiple of the quantum of circulation $\mathcal{K} = \frac{h}{m_n^*}$, where m_n^*, the mass of a neutron Cooper pair, is twice the mass of a neutron. By contrast, the protons in a neutron star form an Abrikosov phase of a type II superconductor [12,13], in which the external magnetic field leads to an array of flux tubes, each carrying a magnetic flux quantum $\Phi_0 = \frac{hc}{q}$, with $q = 2e$ being the charge of a proton Cooper pair. Early studies by Ginzburg and Kirzhnits [14], Wolf [15], and Baym *et al.* [7] laid the foundations for our understanding of neutron superfluidity and proton superconductivity in neutron stars. Also, see the recent review on superfluidity and superconductivity in neutron stars [16] and references therein.

---

[*] Contact author: shuklasanjay771@gmail.com
[†] Contact author: brachet@phys.ens.fr
[‡] Contact author: rahul@iisc.ac.in

Pulsars exhibit sudden increases, known as glitches, in their rotational frequencies [4,5]. The interaction of the pulsar crust with the neutron superfluid may provide an explanation for these glitches, as first suggested by Baym *et al.* [7], and as explored recently by our group in Ref. [3]. Pulsar-glitch observations [4–6] suggest that there is a connection of glitches with the transfer of angular momentum, stored in the quantized vortices of the neutron superfluid, to the solid crust of a pulsar. Various models, such as those based on vortex avalanches [17,18] or superfluid vortex-crust interaction [3,19,20], have been proposed to study the glitching phenomenon.

As we have noted above, a neutron superfluid dominates the outer core of a pulsars. Therefore, Refs. [21,22] have utilized a simple model for a pulsar in which the Gross-Pitaevskii equation (GPE) is used for the neutron superfluid together with a pinning potential for the crust and a rotating container that is defined by a quadratic confining potential. In Ref. [3], our group has removed the confining potential but introduced Newtonian gravity, which leads to a gravitationally collapsed bosonic condensate that displays glitches whose statistical properties are akin to those seen in several pulsars.

Even though protons constitute only about $\simeq 5\%$ of the mass of a pulsar, they play a crucial role in its rich dynamics because the strong magnetic field leads to the formation of an array of flux tubes. The flux tubes in this lattice can interact with the vortices in the neutron superfluid [23]. References [24,25] have examined such interactions, both in equilibrium and out-of-equilibrium conditions, in the 2D and 3D GPE systems, but with (a) a *static ansatz* for the proton flux tubes and (b) *harmonic confinement*. We go beyond approximation (a) and replace the harmonic potential in (b) by Newtonian gravity that leads to a gravitationally collapsed condensate. In particular, we develop a theoretical framework by combining the Maxwell equations for the electromagnetic fields with the 3D Gross-Pitaevskii-Poisson-equation (GPPE) for the neutron superfluid and the real-time-Ginzburg-Landau equation (RTGLE) for the proton-superconductor system. Moreover, we include (i) density-density and (ii) current-current direct interaction between neutron and proton Cooper pairs.

Before going into the details of our calculations, we present the principal results of our study of the coupled GPPE, RTGLE, and Maxwell systems:

(i) We show that the rotation of the proton superconductor leads to a London moment [26], i.e., inside the superconductor there is a uniform magnetic field, whose magnitude depends on the rotation frequency.

(ii) We evolve the magnetic field of the proton flux tubes by using the Maxwell equations; this leads to a precise characterization of the entrainment of protons around neutron vortices, by virtue of which these vortices also become magnetized. This is the first demonstration of such entrainment in the GPPE context.

(iii) If $\Theta > 0$ is the initial angle between the rotation axis and the external magnetic field, then, eventually, the proton-superconductor flux tubes tend to align themselves along the rotation axis. We demonstrate this alignment by calculating the magnetic moment of the proton Cooper pairs.

(iv) We follow the real-time dynamics of the GPPE and RTGLE together with the crust potential, for the illustrative case $\Theta = 0$ and with the neutron and proton Cooper pairs interacting only via the gravitational potential. This gives rise to a collapsed condensate, with a crust angular momentum that displays glitches with signatures of self-organized criticality (SOC) [3,27–30].

The remainder of this paper is organized as follows. In Sec. II, we provide a comprehensive description of the GPPE and RTGLE models. Section III A outlines the units and dimensionless forms of GPPE and RTGLE, accompanied by an elucidation of the pseudospectral method employed for our study. Our results are presented in Sec. IV, followed by a discussion of conclusions in Sec. V.

II. THE MODEL

The total Lagrangian $\mathcal{L}$ governing the dynamics of neutron and proton Cooper pairs within the system is composed of distinct Lagrangians. Section II A delves into $\mathcal{L}_\mathrm{n}$, which encapsulates the dynamics of neutron Cooper pairs. Similarly, Sec. II B focuses on $\mathcal{L}_\mathrm{p}$ describing the proton Cooper pairs, while the electromagnetic field is described by $\mathcal{L}_\mathrm{EM}$ (Sec. II B). The interactions between neutron and proton Cooper pairs are addressed through $\mathcal{L}_\mathrm{np}$ in Sec. II C. Finally, we present the governing equations of motion in Sec. II D by using the total Lagrangian $\mathcal{L}$.

A. Neutron superfluid

In a pulsar, neutrons form Cooper pairs that lead to a superfluid [8,31]. At temperatures below the transition temperature T_λ, these Cooper pairs lead to a Bose-Einstein condensate (BEC), characterized by a macroscopic complex wavefunction ψ_n. The Lagrangian of a weakly interacting rotating BEC in a self-gravitating potential Φ is given by [3]

$$\begin{aligned}\mathcal{L}_\mathrm{n} = {}& \frac{i\hbar}{2}\left(\psi_n^*\frac{\partial\psi_n}{\partial t} - \psi_n\frac{\partial\psi_n^*}{\partial t}\right) - \frac{\hbar^2}{2m_n}|\nabla\psi_n|^2 \\ & - \frac{g}{2}\left(|\psi_n|^2 - \frac{\mu_n}{g}\right)^2 - m_n\Phi|\psi_n|^2 - \frac{1}{8\pi G}(\nabla\Phi)^2 \\ & - V_\theta|\psi_n|^2 + \frac{i\hbar}{2}(\boldsymbol{\Omega}\times\mathbf{r})\cdot(\psi_n\nabla\psi_n^* - \psi_n^*\nabla\psi_n), \qquad (1)\end{aligned}$$

where $g = 4\pi a\hbar^2/m_n$ is the interaction strength between neutron Cooper pairs, a is the s-wave scattering length, m_n

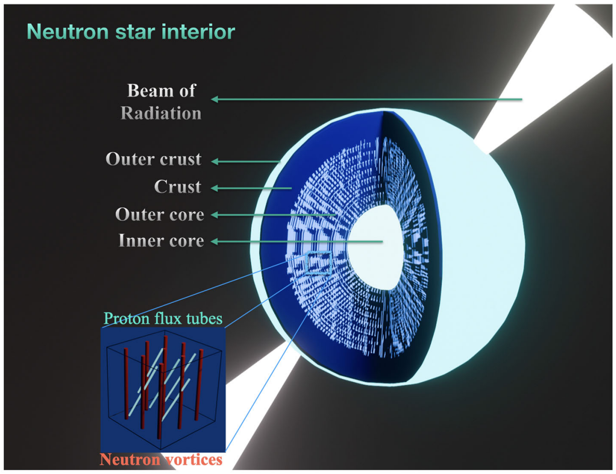

FIG. 1. A schematic diagram (cf. Refs. [32,33]) of the interior of a pulsar (magnetized neutron star). The light-blue luminous central region represents the *inner core*, characterized by ultra-dense matter where neutrons and protons break down into quarks and gluons. Surrounding this core lies the *outer core* (shaded blue-white), composed of a neutron superfluid and proton superconductor, with neutron-superfluid vortices and proton-superconductor flux tubes, respectively (magnified view in the bottom-left inset). The dark-blue crust has a crystalline lattice structure (not shown) and consists of heavy atomic nuclei and free neutrons and free electrons. The neutrons in the crust exist in the form of a superfluid that is threaded by vortices. The glowing white region, often called the outer crust, comprises atomic nuclei and free electrons. The white conical regions show radiation beams emerging from the poles of the pulsar.

and μ_n are, respectively, the mass and chemical potential of neutron Cooper pairs, G is Newton's gravitational constant, and $\mathbf{\Omega}$ is the rotational velocity. Here V_θ represents the crust potential, which is located just above the outer core [see Fig. 1]. This crust potential contains a lattice of atomic nuclei, with each lattice point acting as a pinning center where neutron vortices can be pinned, so they corotate with the crust [details about the crust potential are given in Sec. II E].

B. Proton superconductor

Proton Cooper pairs, which also form in a pulsar, yield a type II superconductor with an Abrikosov flux lattice [7]. This superconducting system can be described by the complex wave function ψ_p, coupled to a vector potential $\mathbf{A}$ and self-gravitating potential Φ, resulting in the following Lagrangian, in which we include the rotational velocity $\mathbf{\Omega}$:

$$\begin{aligned}\mathcal{L}_{\mathrm{p}} = {} & \frac{i\hbar}{2}\left(\psi_p^*\frac{\partial\psi_p}{\partial t} - \psi_p\frac{\partial\psi_p^*}{\partial t}\right) - \frac{1}{2m_p}|D_{\mathbf{A}}\psi_p|^2 \\ & - \frac{\alpha_s}{2}\left(|\psi_p|^2 - \frac{\mu_p}{\alpha_s}\right)^2 - q\phi|\psi_p|^2 - m_p\Phi|\psi_p|^2 - V_\theta|\psi_p|^2 \\ & + \frac{1}{2}(\mathbf{\Omega}\times\mathbf{r})\cdot(\psi_p D_{\mathbf{A}}\psi_p^* + \psi_p^* D_{\mathbf{A}}\psi_p),\end{aligned} \tag{2}$$

where $D_{\mathbf{A}} \equiv [\frac{\hbar}{i}\nabla - q\mathbf{A}]$ is the magnetic gradient operator, m_p is the mass of a proton Cooper pair, α_s is the interaction strength between the proton Cooper pairs, μ_p is the proton chemical potential, $q = 2e$ is the charge of a proton Cooper pair, and ϕ is the electric scalar potential.

The evolution of the vector potential $\mathbf{A}$ follows the Maxwell equations, which can be obtained from the electromagnetic Lagrangian [34]:

$$\begin{aligned}\mathcal{L}_{\mathrm{EM}} = \epsilon_0\Bigg[& -\frac{1}{2}[\mathbf{E}^2 - c^2(\mathbf{B} - \mathbf{B}_{\mathrm{ext}})^2] \\ & + \mathbf{E}\cdot\left(-\nabla\phi - \frac{\partial\mathbf{A}}{\partial t}\right) - c^2(\mathbf{B} - \mathbf{B}_{\mathrm{ext}})\cdot(\nabla\times\mathbf{A})\Bigg],\end{aligned} \tag{3}$$

where $\mathbf{E}$ and $\mathbf{B}$ are the electric and magnetic fields, respectively, $\mathbf{B}_{\mathrm{ext}}$ is the external magnetic field, and c is the speed of light. In the context of neutron stars, $\mathbf{B}_{\mathrm{ext}}$ is the mean internal magnetic field, which reorganizes into flux tubes when the proton subsystem condenses into a superconducting state. This mean magnetic field is subtracted in Eq. (3) so that it only appears in terms of the curl of a uniform field in the Maxwell equation [see Eq. (10)]. If $\langle\mathbf{A}\rangle$ is periodic then $\langle\mathbf{B}\rangle = \langle\nabla\times\mathbf{A}\rangle = 0$, where $\langle.\rangle$ denotes the spatial average. So, in our calculations using periodic boundary conditions, we use $\mathbf{A}$ that is solid-rotationlike at the position of the star and thus controls the mean magnetic field of the star $\mathbf{B}$, which we call $\mathbf{B}_{\mathrm{ext}}$ [see Eq. (28)].

C. Interaction between neutron and proton Cooper pairs

We consider (i) the density-density and (ii) the current-current interactions between the neutron and proton subsystems [24,35] and use the Lagrangian,

$$\begin{aligned}\mathcal{L}_{\mathrm{np}} = \gamma\Bigg\{ & g_{np}|\psi_n|^2|\psi_p|^2 - \frac{\hbar}{4i}(\psi_n\nabla\psi_n^* - \psi_n^*\nabla\psi_n) \\ & \cdot[\psi_p D_{\mathbf{A}}\psi_p^* + \psi_p^* D_{\mathbf{A}}\psi_p]\Bigg\},\end{aligned} \tag{4}$$

where γ is the overall interaction strength, g_{np} is the density-density coupling constant [36]. The current-current interaction, given in the second row, causes neutron-superfluid vortices to drag proton-superconductor flux tubes.

D. Total Lagrangian: Equations of motion

By combining the Lagrangians (1)–(4) we obtain the total Lagrangian,

$$\mathcal{L} = \mathcal{L}_{\mathrm{n}} + \mathcal{L}_{\mathrm{p}} + \mathcal{L}_{\mathrm{EM}} + \mathcal{L}_{\mathrm{np}}. \tag{5}$$

The Euler-Lagrange equations for $\mathcal{L}$ yield the following:

- (i) The GPPE for neutron Cooper pairs (variation with respect to ψ_n^*):

$$i\hbar\frac{\partial\psi_n}{\partial t} = -\frac{\hbar^2}{2m_n}\nabla^2\psi_n - \mu_n\psi_n + g|\psi_n|^2\psi_n + m_n\Phi\psi_n + i\hbar(\mathbf{\Omega}\times\mathbf{r})\cdot\nabla\psi_n + V_\theta\psi_n + \gamma g_{np}|\psi_p|^2\psi_n - \frac{\gamma\hbar}{2i}[\nabla\psi_n\cdot\mathbf{J}_p + \nabla\cdot(\psi_n\mathbf{J}_p)]; \tag{6}$$

here, $\mathbf{J}_p$ is the proton current density:

$$\mathbf{J}_p = \frac{\hbar}{2i}(\psi_p^*\nabla\psi_p - \psi_p\nabla\psi_p^*) - q\mathbf{A}_{\mathrm{eff}}|\psi_p|^2. \tag{7}$$

- (ii) The real-time Ginzburg-Landau-Poisson equation (RTGLPE) for proton Cooper pairs (variation with respect to ψ_p^*):

$$i\hbar\left(\frac{\partial}{\partial t} + \frac{i}{\hbar}q\phi_{\mathrm{eff}}\right)\psi_p = \frac{1}{2m_p}\left(\frac{\hbar}{i}\nabla - q\mathbf{A}_{\mathrm{eff}}\right)^2\psi_p - \mu_p\psi_p + \alpha_s|\psi_p|^2\psi_p + m_p\Phi\psi_p + V_\theta\psi_p + \gamma g_{np}|\psi_n|^2\psi_p + \gamma q(\mathbf{J}_n\cdot\mathbf{A})\psi_p - \frac{\gamma\hbar}{2i}[\mathbf{J}_n.\nabla\psi_p + \nabla\cdot(\mathbf{J}_n\psi_p)]; \tag{8}$$

here,

$$\phi_{\mathrm{eff}} = \phi - \frac{m_p}{2q}\Omega^2 r^2;$$
$$\mathbf{A}_{\mathrm{eff}} = \mathbf{A} + \frac{m_p}{q}(\mathbf{\Omega}\times\mathbf{r});$$
$$\mathbf{J}_n = \frac{\hbar}{2i}(\psi_n^*\nabla\psi_n - \psi_n\nabla\psi_n^*). \tag{9}$$

- (iii) The Maxwell equation for the vector potential $\mathbf{A}$ and Poisson equations for the gravitational potential Φ and the electric scalar potential ϕ:

$$\frac{1}{c^2}\frac{\partial^2\mathbf{A}}{\partial t^2} - \nabla^2\mathbf{A} - \nabla\times\mathbf{B}_{\mathrm{ext}} = \mathbb{P}\left[\frac{q}{m_p c^2\epsilon_0}\mathbf{J}_p - \frac{\gamma q}{c^2\epsilon_0}\mathbf{J}_n|\psi_p|^2\right]; \tag{10}$$

$$\nabla^2\Phi = 4\pi G(m_n|\psi_n|^2 + m_p|\psi_p|^2 - \rho_{\mathrm{bg}}); \tag{11}$$

$$\rho_{bg} = m_n\langle|\psi_n|^2\rangle + m_p\langle|\psi_p|^2\rangle; \tag{12}$$

$$\nabla^2\phi = -\frac{1}{\epsilon_0}(q|\psi_p|^2 - qn_p). \tag{13}$$

With $\gamma = 0$ and without crust potential ($V_\theta = 0$), Eq. (6) has been used extensively in Refs. [37–39] to study self-gravitating BECs at temperature $T = 0$ (by using a Gaussian ansatz for $|\psi_n|^2$). References [40,41] have performed numerical simulations without rotation ($\mathbf{\Omega} = 0$). Furthermore, Ref. [42] has included rotation in the GPPE to study the dynamical properties of BEC dark matter (but still with $\gamma = 0$ and $V_\theta = 0$). In our previous studies, we have used the GPPE to study the formation of compact bosonic objects at finite temperatures [1] and their axionic counterparts, by including a quintic nonlinearity [2]. The imaginary time ($t \to -it$) version of Eq. (8) with $\gamma = 0$, $V_\theta = 0$, and $\Phi = 0$ is the well-known time-dependent Ginzburg-Landau equation [43] whose solutions give type I and type II superconductors. In conventional calculations for superconductors, the term $\nabla\times\mathbf{B}_{\mathrm{ext}}$ in Eq. (10) vanishes because of the uniformity of $\mathbf{B}_{\mathrm{ext}}$, and it appears only as a boundary condition. In our calculations, which use periodic boundary conditions, we consider $\mathbf{B}_{\mathrm{ext}}$ such that it is periodic in the domain; and it reorganizes itself in the form of flux tubes as time progresses. In the context of neutron stars, this corresponds to the mean internal magnetic field.

In writing Eq. (10), we have used the Coulomb gauge $\nabla\cdot\mathbf{A} = 0$. The Helmholtz projector, which has components $\mathbb{P}_{ij} \coloneqq \delta_{ij} - \mathcal{F}^{-1}\frac{k_i k_j}{k^2}\mathcal{F}$, with $\mathcal{F}$ the Fourier transform operator, projects a field onto its divergence-free part; its application in Eq. (10) maintains the Coulomb gauge. In Eq. (11) for Φ, the gravitational potential, the subtraction of the background mean density ρ_{bg} [often called the Jeans Swindle [44]] can be justified either by defining a Newtonian cosmological constant [45] or by accounting for cosmological expansion [44,46]. Furthermore, in Eq. (13) for the scalar potential ϕ, we subtract the mean charge density, qn_p, to maintain charge neutrality in the system. In the context of a neutron star, qn_p corresponds to the background charge coming from electrons.

The important term considering the interaction between neutron and proton Cooper pairs is the last term in Eq. (10), which is of the form $\frac{\gamma q}{c^2\epsilon_0}\mathbf{J}_n|\psi_p|^2$. This term, not considered hitherto in the GPPE and RTGLPE, causes neutron-superfluid vortices to drag proton-superconductor flux tubes, generate an entrained-proton current, because of which the neutron-superfluid vortices become magnetized, as we show below.

E. Crust potential (V_θ)

The region just above the outer core of a neutron star, known as the crust, contains heavy nuclei arranged in a lattice structure. This crust plays a crucial role in models of pulsar glitches. Neutron vortices become pinned to the lattice sites and corotate with the crust. As the crust spins down, the superfluid within remains unaffected because of its zero viscosity. This differential rotation causes vortices to unpin from their pinning sites, thus transferring momentum to the crust and resulting in glitches. Flux tubes are also anchored to the crust by the strong magnetic field, and there is a depletion of the proton cooper pairs. In our model, spherically collapsed neutron and proton condensates contain vortices and flux tubes that are located away from the cubic domain boundary. The crust potential lies just above the condensate, with the magnetic field inside the flux tubes passing through the crust anchoring them. In this section, we model the crust using a Gaussian potential V_θ modulated by equally spaced pinning centers. In the absence of the crust potential V_θ, Eqs. (6)–(13) govern the interplay between neutron-superfluid vortices and proton-superconductor flux tubes in the outer-core region shown in the schematic diagram of Fig. 1. At the level of a minimal model for pulsars [3] the dynamics of this crust is characterized by a single polar angle θ [3] that evolves as follows:

$$
\begin{aligned}
I_c \frac{d^2\theta}{dt^2} &= \frac{1}{N_n}\left(\int d^3x \partial_\theta V_\theta |\psi_n|^2 + \frac{n_n}{n_p}\int d^3x \partial_\theta V_\theta |\psi_p|^2\right) \\
&\quad - \delta \frac{d\theta}{dt}; \\
V_\theta(\mathbf{r}_p) &= V_0 \exp\left[-\frac{(|\mathbf{r}_p| - r_{\text{crust}})^2}{(\Delta r_{\text{crust}})^2}\right]\tilde{V}(x_\theta, y_\theta); \qquad (14)
\end{aligned}
$$

here, I_c is the moment of inertia of the crust, the angle θ represents the angular rotation of the neutron star's crust about the rotation axis, $N_n = \int |\psi_n|^2 d^3x$ is the total number of neutron Cooper pairs, n_n/n_p is the ratio of the number densities of neutrons and protons, and the slowing down of the crust is controlled by the friction coefficient δ. The first two terms on the right-hand side of upper Eq. (14) couple the crust to the superfluid and superconductor, respectively. These terms ensure that the superfluid and superconductor act on the crust. The last term on the right-hand side of upper Eq. (14) represents the friction, which slows down the crust and creates a differential rotation between it and the superfluid. The evolution Eq. (14) for the crust potential can be written in the compact form $I_c\ddot{\theta} = \mathrm{F}_s - \delta\dot{\theta}$, where F_s, the force of the superfluid on the crust, is given by the term in parentheses in the first line of Eq. (14).

We choose $\tilde{V}(x_\theta, y_\theta) = 3 + \cos(n_{\text{crust}} x_\theta) + \cos(n_{\text{crust}} y_\theta)$, with $x_\theta = \cos(\theta)x_p + \sin(\theta)y_p$ and $y_\theta = -\sin(\theta)x_p + \cos(\theta)y_p$ as in Ref. [3]; here, n_{crust} determines the number of pinning sites in the crust, r_{crust} is the radius at which V_θ assumes its maximum value, and Δr_{crust} is the thickness of the crust. We use a 2π-periodic version of the coordinates, namely, $\mathbf{r}_p = (x_p, y_p, z_p)$, which is π-centered, with $z_p = \pi$,

$$
\begin{aligned}
x_p &= -\sum_{n=1}^{10} \exp\left(-\frac{16}{100}n^2\right)(-1)^n \frac{\sin(n(x-\pi))}{n}, \\
\text{and} \quad y_p &= -\sum_{n=1}^{10} \exp\left(-\frac{16}{100}n^2\right)(-1)^n \frac{\sin(n(y-\pi))}{n}. \qquad (15)
\end{aligned}
$$

For the proton superconductor, in the absence of rotation, we have $\mathbf{A}_{\text{eff}} \to \mathbf{A}$ and $\phi_{\text{eff}} \to \phi$ [Eq. (9)]. A superconductor that is subjected to rotation ($\mathbf{\Omega} \neq 0$) and which is in a uniform external magnetic field displays a captivating interplay of quantum phenomena. Consider first a nonrotating type-II superconductor in an external magnetic field; it can display a vortex-lattice phase in which flux tubes are arranged in the form of an Abrikosov lattice [47]; the quantized magnetic flux $\Phi_B = \int \mathbf{A}\cdot d\mathbf{l}$ passes through each vortex. Each of these magnetized vortices contributes a discrete quantum of magnetic flux to the net magnetic field inside the superconductor, which is zero outside the vortices. Next consider a rotating superconductor without an external magnetic field; this displays a uniform magnetic field, known as the London moment [26,48]. (This field is uniform away from the boundary, for distances larger than λ_p, the London penetration depth.) The London moment follows from $\mathbf{A}_{\text{eff}}$ [Eq. (9)] because the RTGLPE [Eq. (8)] has an additional term with a vector potential (the subscript L stands for London)

$$
\mathbf{A}_{\mathrm{L}} = -\frac{m_p}{q}(\mathbf{\Omega} \times \mathbf{r}), \qquad (16)
$$

so that, in the absence of flux tubes, $\mathbf{A}_{\text{eff}} = 0$ inside the superconductor. For a rotating type II superconductor [49], in a uniform magnetic field, there is a critical rotational speed Ω_c^p beyond which vortices (here, proton-superconductor flux tubes) enter the system. The critical Ω_c^p, which follows by minimizing the energy in the rotating frame $E' \equiv E - \mathbf{\Omega}\cdot\mathbf{L}_z$, with $\mathbf{L}_z$ the angular momentum along the rotation axis, is

$$
\Omega_c^p = \frac{\hbar}{m_p \lambda_p^2} \ln\left(\frac{\lambda_p}{\xi_p}\right), \qquad (17)
$$

where ξ_p, and λ_p are, respectively, the superconducting coherence length and the London penetration depth. In the Abrikosov-lattice phase, a London moment ($\propto \mathbf{\Omega}$) is present inside the superconducting together with flux-tube lattice.

III. UNITS AND NUMERICAL METHOD

A. Nondimensionalization

We use the dimensionless forms of Eqs. (6)–(13), which we obtain by using the general reference length L_{ref} and speed V_{ref}. The scaled position $\mathbf{x}$, time t, vector potential $\mathbf{A}$, and scalar potential ϕ are

$$\begin{aligned} \mathbf{x} &= L_{\mathrm{ref}}\mathbf{x}', \\ t &= \frac{L_{\mathrm{ref}}}{V_{\mathrm{ref}}}t', \\ \mathbf{\Omega} &= \frac{L_{\mathrm{ref}}}{V_{\mathrm{ref}}}\mathbf{\Omega}', \\ \mathbf{A} &= \frac{H_{\mathrm{c2}}L_{\mathrm{ref}}}{\kappa}\mathbf{A}', \\ \text{and}\quad \phi &= \frac{L_{\mathrm{ref}}^2}{\tau}\frac{H_{\mathrm{c2}}}{\kappa}\phi', \end{aligned} \tag{18}$$

where H_{c2} is the (zero-temperature) upper critical magnetic field of the superconductor, $\kappa = \frac{\lambda}{\xi_p}$ is the London ratio, and $\tau = \frac{L_{\mathrm{ref}}}{V_{\mathrm{ref}}}$. In Table I, we provide all the parameters and dimensionless ratios that follow from our nondimensionalization. The wave functions are normalized as $\psi_n = \sqrt{n_n}\psi_n'$ and $\psi_p = \sqrt{n_p}\psi_p'$, so the nondimensionalized neutron GPPE, proton RTGLPE, and vector, gravitational, and scalar potential equations are, respectively, (for notational simplicity we now drop the primes that come from nondimensionalization):

$$\begin{aligned} i\frac{\partial\psi_n}{\partial t} = &-\alpha\nabla^2\psi_n + \beta(|\psi_n|^2 - 1)\psi_n + \mathfrak{G}\Phi\psi_n \\ &+ i(\mathbf{\Omega}\times\mathbf{r})\cdot\nabla\psi_n + V_\theta\psi_n + \gamma_p\mathfrak{g}|\psi_p|^2\psi_n \\ &- \frac{\gamma_p\alpha}{i}[\nabla\psi_n\cdot\mathbf{J}_p + \nabla\cdot(\psi_n\mathbf{J}_p)]; \end{aligned} \tag{19}$$

TABLE I. Definitions of all the dimensionless parameters and ratios appearing in Eqs. (19)–(23).

Parameters in Eqs. (19)–(23)	Description
$\alpha = \frac{c_s\xi_n}{\sqrt{2}L_{\mathrm{ref}}V_{\mathrm{ref}}}$	Coefficient of the kinetic term in Eqs. (19) and (20)
$\beta = \frac{c_s L_{\mathrm{ref}}}{\sqrt{2}\xi_n V_{\mathrm{ref}}}$	Coefficient of the nonlinear term in Eqs. (19) and (20)
$\mathfrak{G} = \frac{L_{\mathrm{ref}}^3 2\sqrt{2}\pi G m_n n_n}{V_{\mathrm{ref}}c_s\xi_n}$	Gravitational strength
$\mathfrak{g} = \frac{L_{\mathrm{ref}}g_{np}}{\sqrt{2}\xi_n V_{\mathrm{ref}}c_s m_n m_p}$	Density-density coupling strength
$\frac{n_p}{n_n}$	Number-density ratio (protons to neutrons)
γ	Dimensional interaction strength
$\gamma_n = \gamma m_n n_n$	Interaction coefficient for protons
$\gamma_p = \gamma m_p n_p$	Interaction coefficient for neutrons
$\xi_n = \frac{\hbar}{\sqrt{2m_n g n_n}}$	Coherence length for neutron Cooper pairs
$\xi_p = \frac{\hbar}{\sqrt{2m_p\alpha_s n_p}}$	Coherence length for proton Cooper pairs
λ_p	London penetration depth
$\frac{c}{c_s}$	Ratio of speed of light to speed of sound
$\kappa = \frac{\lambda_p}{\xi_p}$	London ratio
Ω	Dimensionless rotational speed

$$\begin{aligned} &i\left(\frac{\partial}{\partial t} + i\frac{L_{\mathrm{ref}}^2}{\kappa\xi_p^2}\phi_{\mathrm{eff}}\right)\psi_p \\ &= \alpha\left(\frac{\nabla}{i} - \frac{L_{\mathrm{ref}}^2}{\xi_p^2\kappa}\mathbf{A}_{\mathrm{eff}}\right)^2\psi_p + \mathfrak{G}\Phi\psi_p \\ &\quad + \beta\frac{\xi_n^2}{\xi_p^2}(|\psi_p|^2 - 1)\psi_p + V_\theta\psi_p + \gamma_n\mathfrak{g}|\psi_n|^2\psi_p \\ &\quad - \gamma_n\alpha(2\mathbf{J}_n\cdot D_{\mathbf{A}} + i\psi_p\nabla\cdot\mathbf{J}_n); \end{aligned} \tag{20}$$

$$\frac{V_{\mathrm{ref}}^2}{c^2}\frac{\partial^2\mathbf{A}}{\partial t^2} - \nabla^2\mathbf{A} - \nabla\times\mathbf{B}_{\mathrm{ext}} = \mathbb{P}\left[\frac{1}{\kappa}\mathbf{J}_p - \frac{\gamma_n}{\kappa}\mathbf{J}_n|\psi_p|^2\right]; \tag{21}$$

$$\nabla^2\Phi = |\psi_n|^2 + \frac{n_p}{n_n}|\psi_p|^2 - n_{\mathrm{bg}}; \tag{22}$$

$$\nabla^2\phi = -\frac{\beta}{\kappa}\left(\frac{c}{c_s}\right)^2(|\psi_p|^2 - 1). \tag{23}$$

The dimensionless current densities and effective vector and scalar potentials are, respectively:

$$\begin{aligned} \mathbf{J}_n &= \frac{1}{2i}(\psi_n^*\nabla\psi_n - \psi_n\nabla\psi_n^*); \\ \mathbf{J}_p &= \frac{1}{2i}(\psi_p^*\nabla\psi_p - \psi_p\nabla\psi_p^*) - \frac{L_{\mathrm{ref}}^2}{\xi_p^2\kappa}\mathbf{A}_{\mathrm{eff}}|\psi_p|^2; \\ \mathbf{A}_{\mathrm{eff}} &= \mathbf{A} + \frac{\xi_p^2}{L_{\mathrm{ref}}^2}\frac{\kappa}{2\alpha}(\mathbf{\Omega}\times\mathbf{r}); \\ \phi_{\mathrm{eff}} &= \phi - \frac{\xi_p^2}{L_{\mathrm{ref}}^2}\frac{\kappa}{4\alpha}(\Omega^2 r^2). \end{aligned} \tag{24}$$

For the convenience of the reader, we define all the parameters and dimensionless ratios in Table I.

We use pseudospectral direct numerical simulations (DNSs) to solve Eqs. (14) and (19)–(23) in a cubic domain, with side $L = 2\pi$ and N^3 collocation points, and periodic boundary conditions in all three directions. We employ the Fourier expansion for the function $\Psi \equiv (\psi_n, \psi_p, A_x, A_y, A_z, \Phi, \phi)$ as follows:

$$\Psi(\mathbf{x}) = \sum_{\mathbf{k}}\hat{\Psi}_{\mathbf{k}}\exp(i\mathbf{k}\cdot\mathbf{x}), \tag{25}$$

and the 2/3-rule for dealiasing, i.e., we truncate the Fourier modes by setting $\hat{\Psi}_{\mathbf{k}} \equiv 0$ for $|\mathbf{k}| > k_{\max}$ [50,51], with $k_{\max} = [N/3]$. Given current computational resources, it is well-nigh impossible to use such a DNS with astrophysically realistic values (say for a pulsar) for the parameters and ratios in Table I. Nevertheless, as we show below, it is possible to obtain a large body of results that are qualitatively relevant for (a) interactions between proton-superconductor flux tubes and neutron-superfluid vortices and (b) a minimal model for pulsars and their glitches [3].

We will use the imaginary time versions of equations in the initial parts of the results, which can be obtained by using the substitution $t \to -it$ in Eqs. (19)–(20). The imaginary-time version of the Maxwell equation (21) is the following first-order partial differential equation (similar to the vector-potential equation used in the formulation of the time dependent Ginzburg-Landau model of superconductivity [52]):

$$\frac{V_{\mathrm{ref}}^2}{c^2}\frac{\partial \mathbf{A}}{\partial t} - \nabla^2\mathbf{A} - \nabla \times \mathbf{B}_{\mathrm{ext}} = \mathbb{P}\left[\frac{1}{\kappa}\mathbf{J}_p - \frac{\gamma_n}{\kappa}\mathbf{J}_n|\psi_p|^2\right]. \qquad (26)$$

B. Initial conditions

To solve imaginary-time ($t \to -it$) versions of the GPPE (19), the RTGLE (20), and the Maxwell equation (26), we use the following initial conditions:

(i) *ICI1*: The imaginary-time ($t \to -it$) version of GPPE with $\mathbf{\Omega} = 0$ is first evolved by using a uniform density distribution and with small superimposed perturbations. This gives a spherically collapsed condensate. We now use this collapsed state as an initial condition in the same equation but with a small value of $\mathbf{\Omega}$. We keep increasing $\mathbf{\Omega}$ in small steps until we get a collapsed object threaded by vortices.

(ii) *ICI2*: For the RTGLE, we follow the procedure used in *ICI1*, but we insert vortices initially by choosing

$$\psi_{pi} = \psi_{\mathrm{uni}} \times [\cos(kx) + i\cos(ky)]^n, \qquad (27)$$

where ψ_{uni} is a uniform density distribution with small superimposed perturbations. Here, the integer n denotes the multiplicity of a vortex; and k is the number of vortices in the interval $[-\pi/n, \pi/n]$.

(iii) *ICI3*: For the imaginary-time version of the Maxwell equations (26), we use the following initial condition:

$$A_x = -\frac{1}{2} \times y_p \times B_{\mathrm{ext}},$$
$$A_y = \frac{1}{2} \times x_p \times B_{\mathrm{ext}}, \qquad (28)$$

where x_p and y_p are the periodic versions of the coordinates [Eq. (15)] and B_{ext} is the uniform external magnetic field in the z-direction.

IV. RESULTS

Our results are presented in the following subsections:

(i) Section IV A: we solve the imaginary-time versions of Eqs. (19)–(23) without any interactions ($\gamma = 0$), no crust potential ($V_\theta = 0$), and $\Theta = 0$, where Θ is the angle between the rotation axis and external magnetic field. Note that, even if there is no direct interaction between the neutron-superfluid and the proton-superconductor (i.e., $\gamma = 0$), they interact indirectly through the gravitational Poisson equation (22).

(ii) Section IV B: we solve the imaginary-time versions of Eqs. (19)–(23), but with $\gamma \neq 0$, $V_\theta = 0$, and $\Theta = 0$.

(iii) Section IV C: we solve the imaginary-time versions of Eqs. (19)–(23), but with $V_\theta = 0$ and $\Theta = 30°$ and (i) $\gamma = 0$ [Sec. IV C 1] and (ii) $\gamma \neq 0$ [Sec. IV C 2].

(iv) Section IV D: we solve the *real-time* equations (19)–(23) with nonzero crust potential ($V_\theta \neq 0$), no direct interactions ($\gamma = 0$), and $\Theta = 0$. Note that the *imaginary-time* evolution in Secs. IV A–IV C has no dynamical significance; this evolution just provides us with a convenient way of obtaining the equilibrium configuration at very large imaginary time.

A. Imaginary-time study: $\gamma = 0$, $V_\theta = 0$, $\Theta = 0$

We solve imaginary-time ($t \to -it$) versions of Eqs. (19)–(21) together with Eqs. (22) and (23) with $\gamma = 0$, $V_\theta = 0$, and $\Theta = 0$. The imaginary-time version of the Maxwell equation (21) is given in Eq. (26). For all the imaginary-time studies, we start with the initial conditions *ICI1*, *ICI2*, and *ICI3* given in Sec. III B. The neutron star in our model rotates with an angular velocity $\mathbf{\Omega} = \Omega\hat{z}$; for specificity, we choose $\Omega = 2.5$. Both the neutron-superfluid and proton-superconductor subsystems also rotate with this frequency; if we include an external magnetic field $\mathbf{B}_{\mathrm{ext}}$, the proton-superconductor responds directly to it. However, to isolate the effects of the rotation and the external magnetic field, it is useful to study the following three cases: (i) the neutron-superfluid rotates, but not the proton-superconductor, which is in an external magnetic field; (ii) both the neutron-superfluid and the proton-superconductor rotate, but there is no external magnetic field; and (iii) both the neutron-superfluid and the proton-superconductor rotate, and there is an external magnetic field. Clearly, only case (iii) is directly relevant to neutron stars.

Case(i): The neutron condensate rotates [$\mathbf{\Omega} = \Omega\hat{z}$] and the nonrotating proton condensate is in an external magnetic field $\mathbf{B}_{\mathrm{ext}} = B\hat{z}$. In Figs. 2(a)–2(d) we show via contour plots of $|\psi_n|^2$ and $|\psi_p|^2$, respectively, that the neutron condensate is threaded by vortices and the proton-superconductor displays an Abrikosov flux lattice. Each vortex in this lattice carries the quantum of magnetic flux $\Phi_B = \oint \mathbf{A}\cdot d\mathbf{l}$. Initially, the magnetic field is confined near the boundary [Fig. 2(e)]. Eventually these vortices penetrate the condensate [Fig. 2(f)] and each one of them contributes the unit magnetic flux $\Phi_B = \oint \mathbf{A}\cdot d\mathbf{l}$ to the overall magnetic field, which is confined within quantized flux tubes, solely inside the proton superconductor. Initially

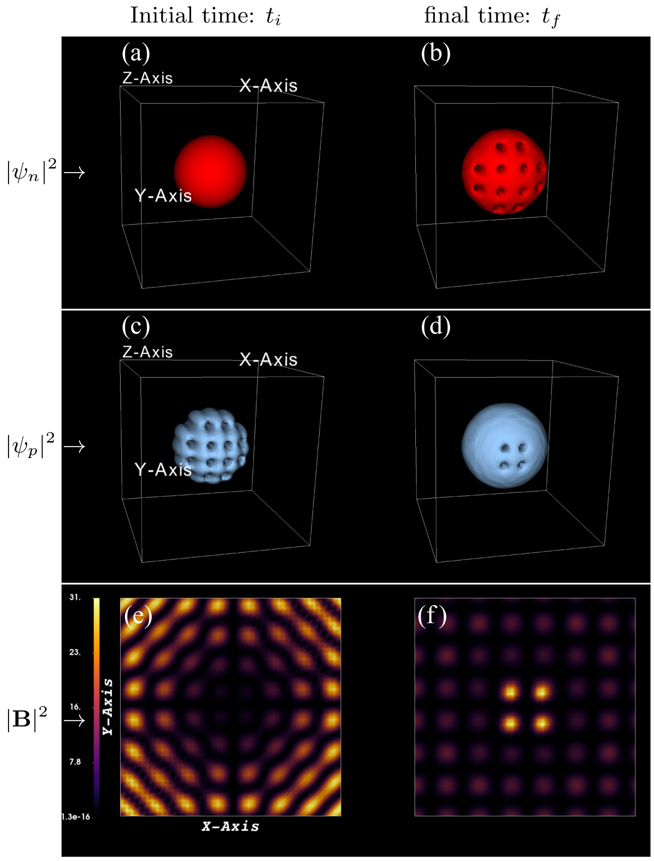

FIG. 2. One-level contour plots of (a),(b) the neutron Cooper-pair density $|\psi_n|^2$ and (c),(d) proton Cooper-pair density $|\psi_p|^2$, obtained by using the imaginary time ($t \to -it$) versions of the GPPE (19) and RTGLPE (20). Pseudocolor plots (e),(f) of the magnetic field $\mathbf{B} = \nabla \times \mathbf{A}$ at the mid-plane $z = L/2$. Here, the neutron condensate rotates with and angular velocity $\mathbf{\Omega} = \Omega\hat{z}$, with $\Omega = 2.5$; the nonrotating proton condensate is placed in an external magnetic field $\mathbf{B}_{\text{ext}} = B\hat{z}$, with $B = 0.8$; neutron and proton Cooper pairs interact only through the gravitational potential (i.e., $\gamma = 0$).

we insert flux tubes inside the proton condensate [Fig. 2(c) and *ICI2* in Appendix III B] because, in the absence of rotation, the system cannot generate flux tubes at $T = 0$.

Case(ii): both the neutron-superfluid and the proton-superconductor rotate [with $\mathbf{\Omega} = \Omega\hat{z}$], but there is no external magnetic field [$\mathbf{B}_{\text{ext}} = 0$]. The neutron condensate is threaded by vortices [Figs. 2(a) and 2(b)], beyond a critical angular velocity, as in Case (i). The behavior of the proton superconductor presents a compelling contrast. For slow rotation, less than a critical Ω_c^p (we use $\Omega = 2.5$ here), the proton superconductor assumes a spherical shape devoid of vortices, as illustrated in Fig. 3(a). Furthermore, within the superconductor, a uniform London field emerges [Fig. 3(c)], first from the superconductor's boundary at the characteristic length scale λ_p, which is the London penetration depth [see Sec. II E]. Any macroscopic rotation of a neutron superfluid results in the formation of quantized vortices; and the formation of flux tubes in a proton superconductor is driven by the magnetic field, not by macroscopic rotation. However, the rotation of a superconductor generates an additional magnetic field known as the London field. It is important to note that, considering realistic parameter values, the magnitude of the London magnetic field is very small for neutron stars (Ref. [13]). However, given the constrained parameter values in our simulations, the London field attains a reasonable finite value. In our simulation with Eq. (16), the magnitude of the dimensionless London field $\mathbf{B}_L = \nabla \times \mathbf{A}_L$ is

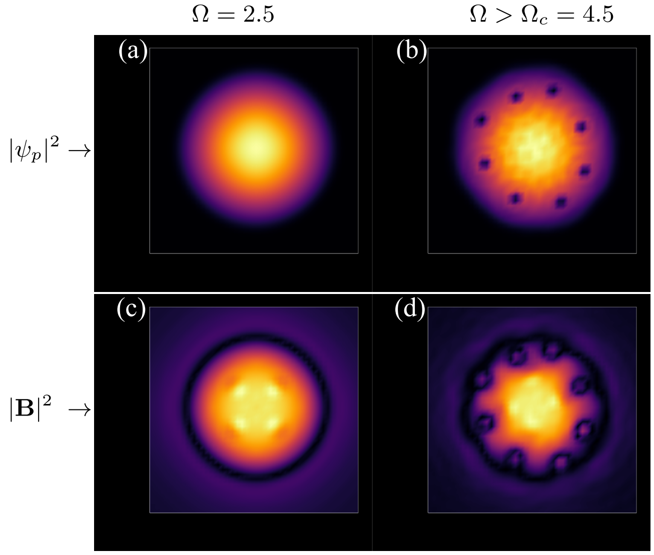

FIG. 3. Pseudocolor plots of (a),(b) the proton Cooper-pair density $|\psi_p|^2$ and (c),(d) the magnetic field $\mathbf{B} = \nabla \times \mathbf{A}$ at the mid plane $z = L/2$. In columns 1 and 2, $\Omega = 2.5$ and $\Omega > \Omega_c = 4.5$, respectively. In these plots, we have $\mathbf{B}_{\text{ext}} = 0$. Neutron and proton Cooper pairs interact only indirectly through the gravitational potential (i.e., $\gamma = 0$).

$$\mathrm{B}_L = \frac{\xi_p^2}{L_{\text{ref}}^2}\frac{\kappa}{\alpha}\Omega \simeq 1.12\Omega. \tag{29}$$

The effect of rotation on the magnetic field distribution around flux tubes can be understood by comparing Figs. 2(f) and 3(d). For a nonrotating proton superconductor in a magnetic field, the field is solely confined inside flux tubes [Fig. 2(f)]. For a rotating proton superconductor, flux tubes enter the system above a critical angular speed Ω_c [compare Figs. 3(c) and 3(d)], and the magnetic field passes through the center of the flux tubes with a finite region around the center devoid of the magnetic field [Fig. 3(d)]. Beyond this finite region, we observe a uniform distribution of the London field. The London magnetic field, a fundamental property of rotating superconductors, has been studied in a hydrodynamical model of a neutron-star interior in Ref. [13]. The generation of this uniform magnetic field is facilitated by the macroscopic London current $\mathbf{J}_{\mathrm{L}}$, which is concentrated near the superconductor's boundary, as we show via 2D vector plots of J_x and J_y in Fig. 4(a).

If $\mathbf{B}_{\text{ext}} = 0$, the rotation is so slow that there are no flux tubes [$\Omega < \Omega_c^p$], and $\gamma = 0$, then we can write Eq. (10) in the steady state as

$$\nabla \times \mathbf{B} = \frac{q}{m_p c^2 \epsilon_0}\mathbf{J}_s - \frac{q n_p}{c^2 \epsilon_0}(\boldsymbol{\Omega} \times \mathbf{r}), \tag{30}$$

where $n_p = |\psi_p|^2$. We now use the London equation

$$\nabla \times \mathbf{J}_s = -\frac{n_p q}{m_p}\mathbf{B}, \tag{31}$$

with $\mathbf{J}_s = m_p n_p \mathbf{v}$, to obtain

$$\nabla \times \nabla \times \mathbf{v} = -\frac{1}{\lambda_p^2}(\mathbf{v} - \boldsymbol{\Omega} \times \mathbf{r}), \tag{32}$$

where $\lambda_p = \sqrt{\frac{m_p c^2 \epsilon_0}{q n_p^2}}$ is the London penetration depth. [A similar relation has been used in Ref. [53] but for a multicomponent superconductor.] If we assume that the density distribution is spherically symmetric, then the proton superconductor has only the azimuthal component $\mathbf{v} = v\mathbf{e}_\phi$, so, by solving Eq. (32), we get

$$\mathbf{v} = \left[\Omega r + \frac{C}{r^2}\left(\sinh\left(\frac{r}{\lambda_p}\right) - \frac{r}{\lambda_p}\cosh\left(\frac{r}{\lambda_p}\right)\right)\right]\mathbf{e}_\phi, \tag{33}$$

whence we obtain the radial component B_r of the magnetic field by using Eqs. (33) and (31):

$$\mathrm{B}_r = \frac{m_p}{q}\left[2\Omega + \frac{2C}{r^3}\left(\sinh\left(\frac{r}{\lambda_p}\right) - \frac{r}{\lambda_p}\cosh\left(\frac{r}{\lambda_p}\right)\right)\right]. \tag{34}$$

We determine the constant C by demanding $\mathrm{B}_{r=\mathrm{R}} = 0$, where R is the radius of the spherical condensate, because $\mathbf{B}_{\text{ext}} = 0$. Finally, we get

$$\frac{\mathrm{B}_r}{\mathrm{B}_L} = 1 - \frac{1}{(r/\mathrm{R})^3}\frac{\sinh\left(\frac{r}{\mathrm{R}}\chi\right) - \frac{r}{\mathrm{R}}\chi\cosh\left(\frac{r}{\mathrm{R}}\chi\right)}{\sinh(\chi) - \chi\cosh(\chi)}, \tag{35}$$

where $\chi = \frac{\mathrm{R}}{\lambda_p}$, which we show via dashed lines in Fig. 4(c) for two representative values of χ. The solid lines in Fig. 4(c) give the results of our DNS, which agree well with the results of our analytical approximation [Eq. (35)]. We observe that, for large value of χ (small λ_p), the internal magnetic field is comparable to the London field B_L; and it decreases as we decrease χ.

Upon increasing the angular velocity Ω beyond $\Omega_c^p \simeq 4.5$ [see Eq. (17)], vortices begin to penetrate the proton superconductor, as we show in Fig. 3(b). Each of these vortices carries a quantum of magnetic flux $\Phi_\Omega = \oint(\boldsymbol{\Omega} \times \mathbf{r}) \cdot d\mathbf{l}$, which is the flux because of the uniform London field B_L within the superconductor [Fig. 3(d)]. Our DNS provides valuable insights into the dynamic interplay between rotation, vortices, and the London field in the proton superconductor. As vortices penetrate the condensate [49], they reduce the uniform magnetic field through the system [54]. The distribution of currents, crucial for generating and sustaining this magnetic field, is revealed by the 2D vector plots of J_x and J_y in Fig. 4(b). Note that these currents are concentrated near the superconductor's boundary and around the vortices.

Case(iii): Both the neutron and proton condensates rotate with $\boldsymbol{\Omega} = \Omega\hat{z}$; and the proton condensate is subjected to an external magnetic field $\mathbf{B}_{\text{ext}} = B\hat{z}$. The equilibrium state of the neutron condensate resembles that of Case (ii), with vortices penetrating the system beyond the neutron critical angular velocity Ω_c^n. The proton condensate manifests a London field B_L as in Case (ii). In Figs. 5(a) and 5(b) we present blue-scale plots of the magnetic field $\mathbf{B} = \nabla \times \mathbf{A}$, in the plane $z = L/2$ and at initial t_i and final t_f representative (imaginary) times; these plots show neutron vortices and proton flux tubes in red and yellow contours, respectively. We visualize these vortices and flux tubes via plots of the

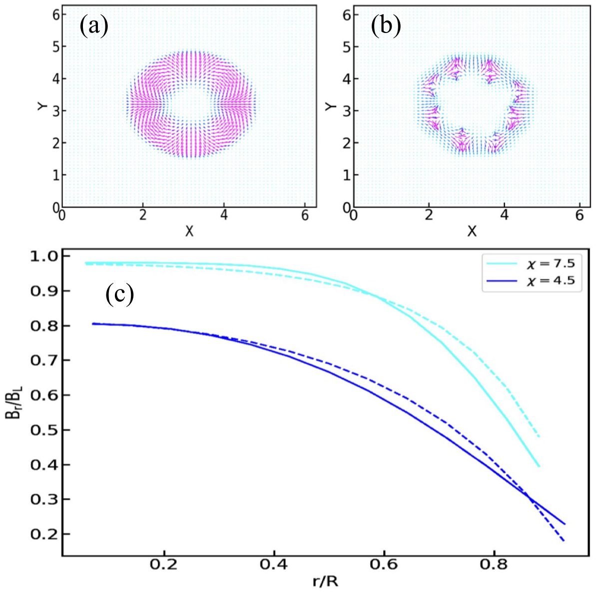

FIG. 4. Two-dimensional (2D) vector plots of the proton Cooper-pair current densities J_x and J_y for (a) $\Omega = 2.5$ and (b) $\Omega > \Omega_c = 4.5$. (c) The magnitude of the radial component of the magnetic field $\mathbf{B} = \nabla \times \mathbf{A}$, normalized by the London magnetic field B_L, plotted as a function of the distance r/R from the center of the superconductor, where R is the radius of the spherical proton condensate. The solid curve is from the imaginary-time DNS of Eqs. (19)–(23) and the dashed curve is the analytical relation (35) for two values of $\chi = \frac{R}{\lambda_p}$, with λ_p the London penetration depth of the superconductor.

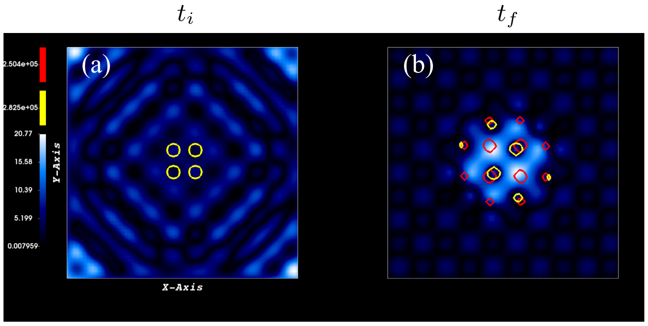

FIG. 5. Pseudocolor plots, at the plane $z = L/2$, illustrating the magnetic field $\mathbf{B} = \nabla \times \mathbf{A}$ in blue at (a) initial t_i and (b) final t_f (imaginary) times, with neutron vortices and proton flux tubes indicated by red and yellow contours, respectively. The vortices and flux tubes are the contour plots of the pseudovorticity $\omega_{\mathrm{p}} = |\nabla \times (\rho \mathbf{v})|$, where ρ is the density and $\mathbf{v}$ is the velocity of the superfluid or superconductor. Both neutron and proton subsystems rotate with $\Omega = 2.5$; and the external magnetic field is $B_{\mathrm{ext}} = 0.8$.

pseudovorticity $\omega_{\mathrm{p}} = |\nabla \times (\rho \mathbf{v})|$, where ρ is the density and $\mathbf{v}$ is the velocity field of the superfluid neutrons or superconducting protons. The velocity field is calculated using the following:

$$\mathbf{v}_{\mathrm{n,p}} = \frac{\hbar}{\rho_{\mathrm{n,p}}} \frac{\psi^*_{\mathrm{n,p}} \nabla \psi_{\mathrm{n,p}} - \psi_{\mathrm{n,p}} \nabla \psi^*_{\mathrm{n,p}}}{2i}, \tag{36}$$

where (n,p) refers to neutron and proton Cooper pairs, respectively.

At the initial (imaginary) time t_i we include proton flux tubes (yellow) in the initial condition [Fig. 5(a)]; the magnetic field is concentrated near the boundary of the simulation box. In the equilibrium state, neutron vortices (in red) enter the condensate and organize themselves in the manner depicted in Fig. 5(b). Even though $\gamma = 0$, i.e., there is no direct interaction between the two components, the neutron-superfluid vortices and proton-superconductor flux tubes come close together, as we show in Fig. 5(b). This effective attraction follows from the coupling induced by the Poisson equation for gravitational potential [Eq. (11)].

It is also important to note that the sizes of vortices in Fig. 5 are different. This can be explained using the pseudovorticity $\omega_{\mathrm{p}} = \nabla \times (\rho \mathbf{v})$, which can be rewritten as

$$\omega_{\mathrm{p}} = \rho \nabla \times \mathbf{v} + (\nabla \rho) \times \mathbf{v}. \tag{37}$$

For a uniform density distribution, such as in harmonic confinement, the second term in Eq. (37) is very small because $\nabla \rho$ is negligible, resulting in vortices of similar sizes throughout the condensate. However, for the self-gravitating case, the density decreases as we move away from the center. This creates a negative density gradient towards the edge, causing ω_{p} to become small and resulting in smaller vortex sizes at the boundary.

B. Imaginary-time study: $\gamma \neq 0$, $V_\theta = 0$, $\Theta = 0$

We examine the interacting case of $\gamma \neq 0$ [in addition to the gravitational-potential-induced coupling in Case (iii)]. Consider first neutron-proton density-density interactions; their effective strength follows from the first term in the interaction Lagrangian (4):

$$g' = g_{np} |\psi_n|^2 |\psi_p|^2. \tag{38}$$

For attractive (repulsive) couplings $g' < 0$ ($g' > 0$), the density minima of neutron-superfluid vortices and proton-superconductor flux tubes align (the maximum of the neutron-superfluid density aligns with the proton flux tubes). (A similar analysis has been conducted in Ref. [24] without a gravitational interaction.) Given that the gravitational interaction is inherently attractive, the attractive case ($g' < 0$) only promotes this alignment; if we start with the same initial condition as in Fig. 5(a), we obtain the final equilibrium state, shown in Fig. 6(a), with overlapping density minima of the neutron-superfluid vortices in red and of proton-superconductor flux tubes in yellow [as in Fig. 5(b), with only gravitation-induced interactions]. In contrast, if $g' > 0$, the interplay between the repulsive density-density interaction and the attractive gravitational interaction is such that cores do not overlap, as evident in Fig. 6(b).

We now incorporate the current-current interaction in the Lagrangian (4). This leads to the entrainment of the proton-superconductor current because of the term $\frac{\gamma q}{c^2 \epsilon_0} \mathbf{J}_n |\psi_p|^2$ in the vector potential (10). This introduces a combination of gravitational, negative density-density ($g' < 0$), and positive current-current interactions, whose effects we investigate by starting with the same initial condition as in Fig. 5(a). As imaginary time progresses, neutron-superfluid vortices (in red) and proton-superconductor flux tubes (in yellow) tend to merge and the minima of neutron and proton densities overlap because of the gravitational and negative density-density interaction [see Fig. 6(c)]. This entrainment causes neutron-superfluid vortices to drag proton-superconductor flux tubes and induces a magnetic field inside these vortices. This is clearly visible as intense blue spots in Fig. 6(c), inside vortices that do not overlap with proton-superconductor flux tubes. To illustrate the generation of this entrainment-induced magnetic field, we plot the magnetic-field energy $\mathrm{E_B(t)} = |\mathbf{B}_{\mathrm{ext}} - \nabla \times \mathbf{A}|^2$ versus imaginary time t in Fig. 6(d) both with (blue curve) and without (cyan curve) current-current interaction. In the latter case $\mathrm{E_B(t)}$ is higher than in the former at large t.

C. Angle between $\mathbf{B}_{\mathrm{ext}}$ and $\boldsymbol{\Omega}$

So far we have examined cases with aligned $\mathbf{B}_{\mathrm{ext}}$ and $\boldsymbol{\Omega}$, i.e., $\Theta = 0$. We turn now to $\Theta > 0$, which is the case in most pulsars.

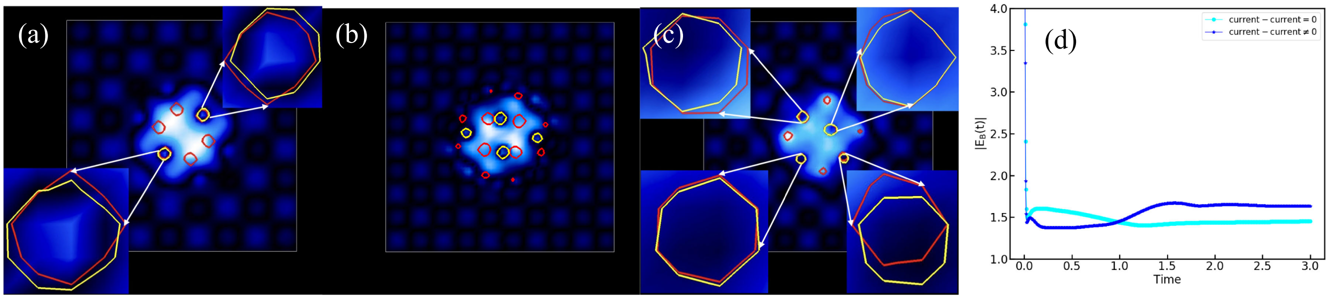

FIG. 6. Pseudocolor plots, at plane $z = L/2$, illustrating the magnetic field $\mathbf{B} = \nabla \times \mathbf{A}$ in blue [at equilibrium, i.e., the final imaginary time in our DNS], with neutron vortices and proton flux tubes shown via red and yellow contours, respectively, for (a) gravitational and attractive ($g' < 0$) density-density interactions, (b) gravitational and repulsive ($g' > 0$) density-density interactions, (c) gravitational, attractive density-density, and also current-current interactions. (d) Imaginary-time series plots of the magnetic-field energy $\mathrm{E_B} = |\mathbf{B}_{\mathrm{ext}} - \nabla \times \mathbf{A}|^2$ for zero current-current interaction ($\gamma = 0$) in cyan and nonzero current-current interaction ($\gamma \neq 0$) in blue. Both neutron and proton subsystems rotate with $\Omega = 2.5$; and the external magnetic field is $B_{\mathrm{ext}} = 0.8$. The vortices and flux tubes are the contour plots of the pseudovorticity $\omega_{\mathrm{p}} = \nabla \times (\rho \mathbf{v})$, where ρ is the density and $\mathbf{v}$ is the velocity of the superfluid or superconductor.

1. No interactions: $\gamma = 0$, $V_\theta = 0$, and $\Theta = 30°$

As in Case (i) Sec. IV A we study a neutron condensate that rotates [$\mathbf{\Omega} = \Omega\hat{z}$] and a nonrotating proton condensate in an external magnetic field $\mathbf{B}_{\mathrm{ext}} = B(\hat{z}\cos\Theta + \hat{y}\sin\Theta)$. We examine the case with no direct interactions, i.e., $\gamma = 0$, no crust potential, i.e., $V_\theta = 0$, and the representative values $\Theta = 30°$ and $\Omega = 2.5 > \Omega_c^n$, so vortices enter the neutron condensate, and the proton condensate is stabilized with an Abrikosov lattice.

In Fig. 7(a), we show a one-level red contour plot of the neutron-superfluid vortices at the final imaginary time; these are aligned along the z-axis. By contrast, the proton-superconductor flux tubes, illustrated by cyan contour plots in Fig. 7(b), form an Abrikosov lattice, have their axes tilted at a fixed angle of $\Theta = 30°$ relative to the z-axis; the magnetic field manifests itself solely within these flux tubes [Fig. 7(c)].

We now consider the counterpart of Case (ii) Sec. IV A; both neutron and proton condensates rotate with an angular velocity $\mathbf{\Omega} = \Omega\hat{\mathbf{z}}$ and there is no external magnetic field [$\mathbf{B}_{\mathrm{ext}} = 0$]. Vortices, oriented along the z-axis, thread the neutron condensate. At small values of the imaginary time t, the proton-superconductor flux tubes are oriented at an angle $\Theta = 30°$ [Fig. 8(a)]. As t increases, these flux tubes try to align themselves along the rotation axis z [Fig. 8(b)], and they do so ultimately [Fig. 8(c)]. This alignment is facilitated by the absence of an external magnetic field, which tends to counteract this reorientation. We also

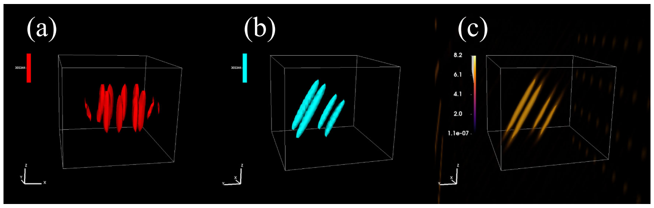

FIG. 7. One-level contour plots of $(\nabla \times (\rho v))^2$ for (a) neutron-superfluid vortices, and (b) proton-superconductors flux tubes at the final imaginary time. (c) Volume plot (final imaginary time) of the magnetic field $\mathbf{B} = \nabla \times \mathbf{A}$. In these plots, the neutron condensate rotates with angular velocity $\mathbf{\Omega} = \Omega\hat{z}$, with $\Omega = 4.0$, and a nonrotating proton condensate; there is an external magnetic field $B_{\mathrm{ext}} = 0.8$ that makes an angle $\Theta = 30°$ with the z-axis. Both species interact only through the gravitational potential.

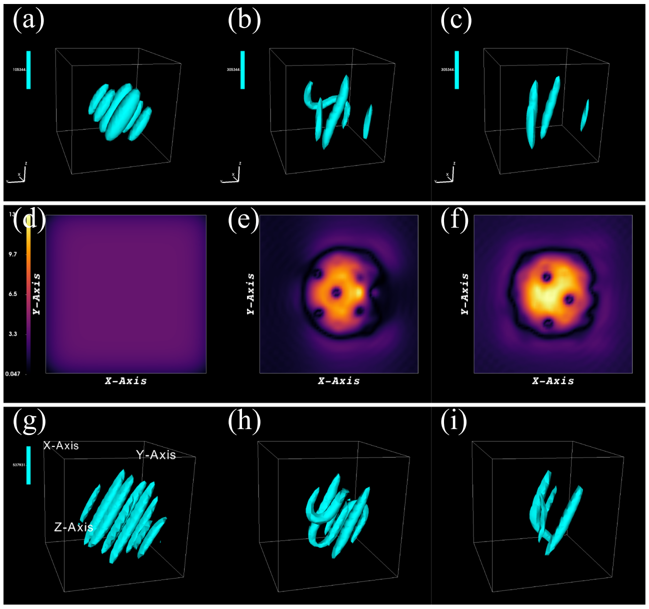

FIG. 8. (a)–(c) One-level contour plots of $(\nabla \times (\rho v))^2$ for proton flux tubes and (d)–(f) pseudocolor plots of the magnetic field $\mathbf{B}$ at the midplane ($z = L/2$) at three representative imaginary times. Both neutron and proton subsystems rotate with the angular velocity $\mathbf{\Omega} = 4.0\hat{z}$; and $\mathbf{B}_{\mathrm{ext}} = 0$. (g)–(i) One-level contour plots of $(\nabla \times (\rho v))^2$ for proton flux tubes with $\mathbf{\Omega} = 4.0\hat{z}$; and $\mathbf{B}_{\mathrm{ext}} = 0.8$. At the initial imaginary time in (a), the proton flux tubes make an angle $\Theta = 30°$ with the z-axis. Both species interact only through the gravitational potential.

observe the generation of a London magnetic field B_L inside the proton condensate [Figs. 8(d)–8(f)].

Finally we consider the counterpart of Case (iii) Sec. IV A; both neutron and proton condensates rotate [$\mathbf{\Omega} = \Omega\hat{\mathbf{z}}$] and there is an external uniform magnetic field $\mathbf{B}_{\mathrm{ext}}$, as in a pulsar, but with interactions solely through the gravitational potential. At small values of the imaginary time t [Fig. 8(g)], the proton-supercondcutor flux tubes are aligned at an angle $\Theta = 30°$ with the z-axis, and the magnetic field is concentrated primarily outside the condensate. As t increases, the proton flux tubes try to orient themselves along the rotation axis [Fig. 8(h)], but $\mathbf{B}_{\mathrm{ext}}$ resists this alignment. Ultimately, these proton-superconductor flux tubes exhibit frustration [Fig. 8(i)] as they try both to align globally with the rotation axis and to adhere to $\mathbf{B}_{\mathrm{ext}}$, which makes an angle $\Theta = 30°$ with the z-axis. This frustration is akin to the glassy behavior of flux tubes, studied in Ref. [24], without gravity but with a quadratic confining potential. In the next subsection we go beyond the study of Ref. [24] by incorporating the full Maxwell equations that lead to entrainment.

2. *Nonzero interactions: $\gamma \neq 0$, $V_\theta = 0$, and $\Theta = 30°$*

Consider now the counterpart of Sec. IV B, i.e., direct interaction ($\gamma \neq 0$) between neutron and proton condensates. We first examine attractive density-density interactions [Eq. (38)], so $g' < 0$. We show the evolution (in imaginary-time t) of the proton-superconductor flux tubes and the magnetic field in Figs. 9(a)–9(c). At the initial time $t = 0$, the proton flux tubes are oriented at an angle $\Theta = 30°$ with respect to the z-axis [Fig. 9(a)]. As t increases, these flux tubes exhibit a rapid realignment with the rotation axis because of the combined gravitational and attractive density-density interactions [Figs. 9(b)–9(c)].

To obtain entrainment, we must introduce the current-current interactions [the second term in Eq. (4)]. The proton flux tubes evolve in imaginary time t as in the previous case with attractive density-density interactions. However, the current-current interaction, $\frac{\gamma q}{c^2\epsilon_0}\mathbf{J}_n|\psi_p|^2$ in the vector potential (10), leads to an entrained proton-superconductor current. This entrainment results in an induced magnetic field inside the neutron-superfluid vortices [gray and red isosurfaces, respectively, in Fig. 10].

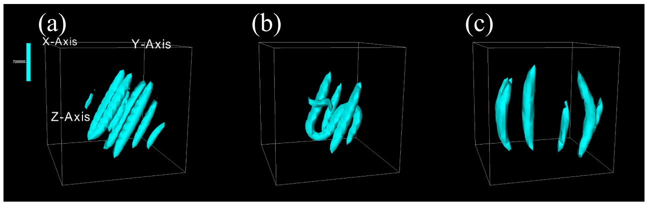

FIG. 9. One-level contour plots of $(\nabla \times (\rho v))^2$ for proton flux tubes at three representative imaginary times in (a)–(c). Both neutron and proton subsystems rotate with the angular velocity $\mathbf{\Omega} = \Omega\hat{z}$, where $\Omega = 4.0$; and $B_{\mathrm{ext}} = 0.8$, which makes an angle $\Theta = 30°$ with the z-axis. Furthermore, we have gravitational and attractive density-density ($g' < 0$) interactions [first term in Eq. (4)] between neutron and proton Cooper pairs.

D. Real-time evolution

We now delve into the real-time equations (19)–(23). We first follow the dynamics of the alignment of proton-superconductor flux tubes with the rotation axis [Fig. 9]. We begin with the configuration of vortices (cyan) and flux tubes (red) shown in Fig. 11(a), which we obtain as the equilibrium state of the imaginary-time versions of Eqs. (19)–(21). The axes of rotation and the magnetic moment $\mathbf{m}$ make an angle χ [see the schematic diagram in Fig. 11(b)]; we define them as follows:

$$\mathbf{m} = \frac{1}{2}\int \mathbf{r} \times \mathbf{J}_p dV; \tag{39}$$

$$\cos(\chi) = \frac{\mathbf{\Omega} \cdot \mathbf{m}}{|\mathbf{\Omega}||\mathbf{m}|}. \tag{40}$$

The angle χ depends on time t; for considerable lengths of time it shows minor fluctuations, but, occasionally, it changes dramatically, as we show in Fig. 11(c) via a plot of $\cos(\chi)$ versus t. The sudden change in $\cos(\chi)$, from positive to negative values, indicates that the magnetic moment undergoes reversals, which are familiar in many other hydrodynamical [55,56], dynamo [57–59], geomagnetic [60–62], and astrophysical [63–65] settings. Measurements for several pulsars [66] indicate that $0° \leq \chi \leq 90°$; e.g., the pulsar (PSR

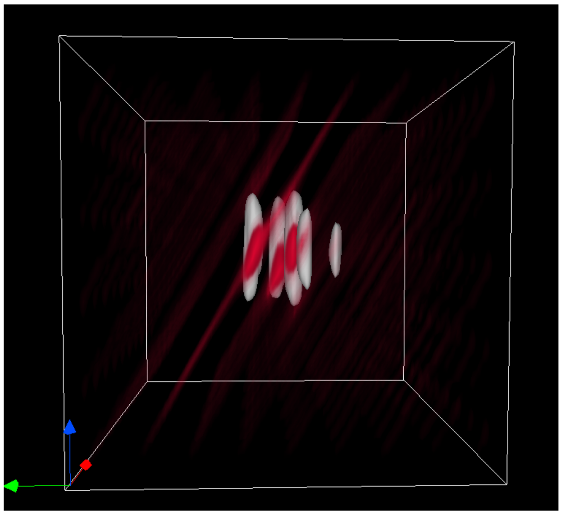

FIG. 10. One-level contour plots of $(\nabla \times (\rho v))^2$ for neutron-superfluid vortices, at the final imaginary time with a superimposed volume plot of the magnetic field $\mathbf{B}$ at the final time. Both neutron and proton subsystems rotate with the angular velocity $\mathbf{\Omega} = \Omega\hat{z}$, where $\Omega = 4.0$; and $B_{\mathrm{ext}} = 0.8$, which makes an angle $\Theta = 30°$ with the z-axis. Gravitational and other interaction terms are included [Eq. (4)].

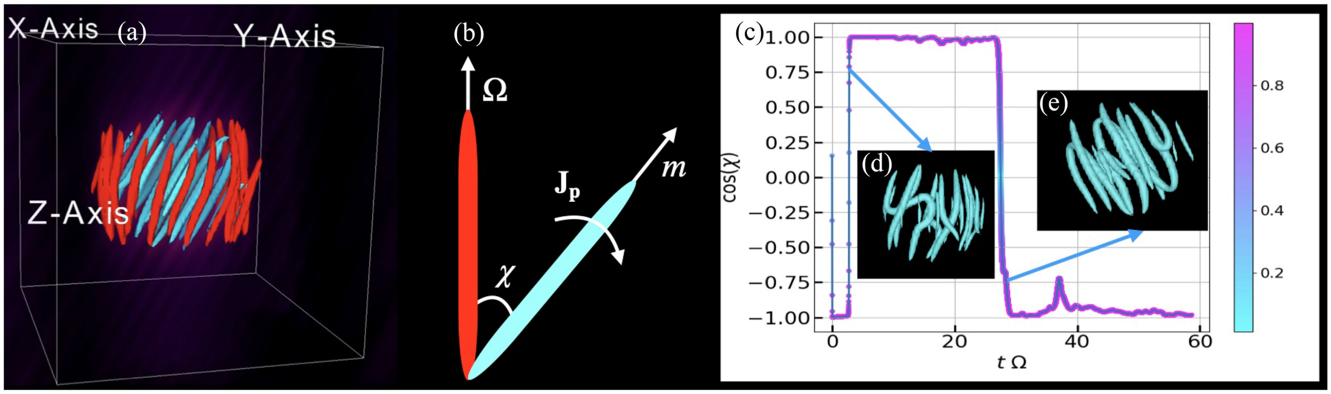

FIG. 11. Real-time evolution: (a) One-level contour plot of $(\nabla \times (\rho v))^2$ for neutron vortices (in red) and proton flux tubes (in cyan) at the initial time. (b) Schematic diagram showing the angle χ between the rotation axis and the magnetic moment [Eq. (39)]. (c) The evolution of the angle χ with time. Both neutron and proton subsystems rotate with angular velocity $\mathbf{\Omega} = \Omega\hat{z}$, where $\Omega = 4.0$; and $B_{\text{ext}} = 0.8$, which makes an angle $\Theta = 30°$ with the z-axis. Insets (d) and (e) show illustrative proton flux-tube configurations before and after the reversal.

B1055-52) is an aligned rotator, whereas another (PSR B1702-19) is an orthogonal rotator; the time scales of these observations are such that, for any given pulsar, χ has a steady, time-independent value.

In our minimal model the crust potential V_θ is a function of a single polar angle θ whose dynamics is given by Eq. (14). To study the interplay of crust, neutron-superfluid, and proton-superconductors, we use Eqs. (19)–(23) along with Eq. (14) and initial conditions that we obtain from the equilibrium states of imaginary-time studies of the previous sections, with the same angular velocity $\Omega = \frac{d\theta}{dt}$ for the crust, the neutron condensate, and the proton condensate. For purposes of illustration, we consider $\Theta = 0$, i.e., the angle between the rotation axis and the magnetic field is zero. The neutrons and protons interact only through the gravitational potential via the Poisson equation ($\gamma = 0$).

In Figs. 12(a)–12(c), we show isosurface plots of the crust potential in blue, isosurfaces of neutron-superfluid vortices in red, and proton-superconductor flux tubes in cyan at three representative times. At the initial time step [Fig. 12(a)], the system features 12 neutron vortices and 6 proton flux tubes. Given the parameters of our simulation, the proton-superconductor flux tubes are more effectively pinned by the crust potential than neutron-superfluid vortices, in part because of the anchoring of the flux tubes to the strong external magnetic field $\mathbf{B}_{\text{ext}}$. Over the duration of the simulation presented in Figs. 12(a)–12(c), the number of neutron-superfluid vortices reduces by a factor of 2 but the number of proton flux tubes remains unchanged. Both superfluid vortices and proton-superconductor flux tubes undergo differential rotation because of the friction coefficient α in Eq. (14) for the polar angle.

The angular momentum of the crust is given as $\mathrm{J}_c = I_c d\theta/dt$, with I_c is the moment of inertia of the crust [see the Appendix for details]. The temporal evolution of J_c is complicated because of the subtle interplay between the

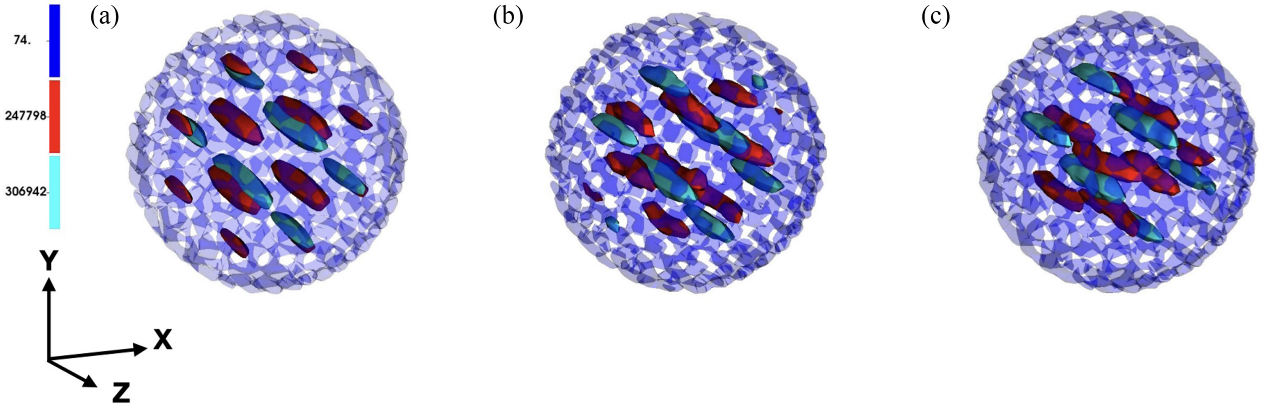

FIG. 12. One-level contour plots of the crust potential together with the neutron vortices (in red) and proton flux tubes (in cyan) at three different times in (a), (b), and (c) obtained by using the real-time GPPE [Eq. (19)] and RTGLE [Eq. (20)]. Both neutron and proton subsystems rotate with an angular velocity $\mathbf{\Omega} = \Omega\hat{z}$, where $\Omega = 4.0$; and $B_{\text{ext}} = 4.0$, which is along the z-axis.

friction, which slows down the crust, and the angular momentum in the neutron-superfluid vortices. When such a vortex is ejected from the pulsar, its angular momentum is transferred to the crust. Some neutron vortices linger close to proton-superconductor flux tubes because of the Poisson-equation-induced gravitational attraction between them. This also affects the time-dependence of J_c. Finally, we have an effective stick-slip dynamics for J_c that displays glitches whose statistics has properties that are akin to those seen in several pulsars and which yield pulsar glitches [3,4,6,67]. We observe small quasioscillatory structures in the time series of J_c. This occurs because we use the periodic version of coordinates (x_p, y_p) defined in Eq. (15). It is also important to note that, in our model, the crust potential rotates with the superfluid when vortices are pinned; however, when a vortex becomes unpinned, the crust experiences a sudden decrease in its angular momentum, followed by an increase in the angular momentum as the unpinned vortex moves from the condensate to the crust, thus transferring its angular momentum.

We now examine the analogs of pulsar glitches in our model, by following the methods developed in Ref. [3]. In particular, we present the time series of the angular momentum $(\mathrm{J}_c - \mathrm{J}_{c_0})/\mathrm{J}_{c_0}$ of the crust in Fig. 13(a). This time series of $(\mathrm{J}_c - \mathrm{J}_{c_0})/\mathrm{J}_{c_0}$ exhibits characteristic features that are associated with SOC [27–30], which we have explored, in the context of gravitationally collapsed boson stars, in our earlier work [3]. Figures 13(b)–13(d) present expanded views of specific segments [indicated by black boxes] of the time series in Fig. 13(a). From the time dependence of J_c, we observe that the crust can either lose angular momentum to the superfluid or can gain angular momentum from it, because of the stick-slip dynamics mentioned above.

To characterize SOC, we quantify the statistics J_c as follows. We measure (a) the event size $\Delta\mathrm{J}_c$, which is the difference between successive minima and maxima in J_c, (b) the event-duration time t_{ed}, which is the time difference between successive minima and maxima of $\mathrm{J}_c(t)$, and (c) the waiting time t_w, which is the time between successive maxima in $\mathrm{J}_c(t)$. We then obtain cumulative probability distribution functions (CPDFs) of $\Delta\mathrm{J}_c$, t_{ed}, and t_w; as in Ref. [3], the former two CPDFs exhibit power-law tails, whereas the last has an exponential tail. In Fig. 13(e), we plot the CPDF $Q(\Delta\mathrm{J}_c/\mathrm{J}_{c_0})$; it scales as $Q(\Delta\mathrm{J}_c/\mathrm{J}_{c_0}) \sim (\Delta\mathrm{J}_c/\mathrm{J}_{c_0})^{\beta}$, within the gray-shaded region. Therefore, the corresponding probability distribution function (PDF) scales as $P(\Delta\mathrm{J}_c/\mathrm{J}_{c_0}) \sim (\Delta\mathrm{J}_c/\mathrm{J}_{c_0})^{\beta-1}$; for our representative run, we obtain the scaling exponent $\beta = 0.86 \pm 0.15$, by using local-slope analysis. The CPDF of t_{ed} shows the power law $Q(t_{\mathrm{ed}}\Omega) \sim (t_{\mathrm{ed}}\Omega)^{\gamma_t}$ in the gray-shaded region of Fig. 13(f), with an exponent $\gamma_t = 2.5 \pm 0.2$ for our run. The CPDF of t_w shows the exponential form $Q(t_w\Omega) \sim \exp(-6.5 t_w\Omega)$ [Fig. 13(f)]. The qualitative forms of these CPDFs is similar to those seen in experiments, as has been noted in Ref. [3], which uses the GPPE system without the proton superconductor and the Maxwell equations that we include. The values of the exponents β and γ lie close to those that have

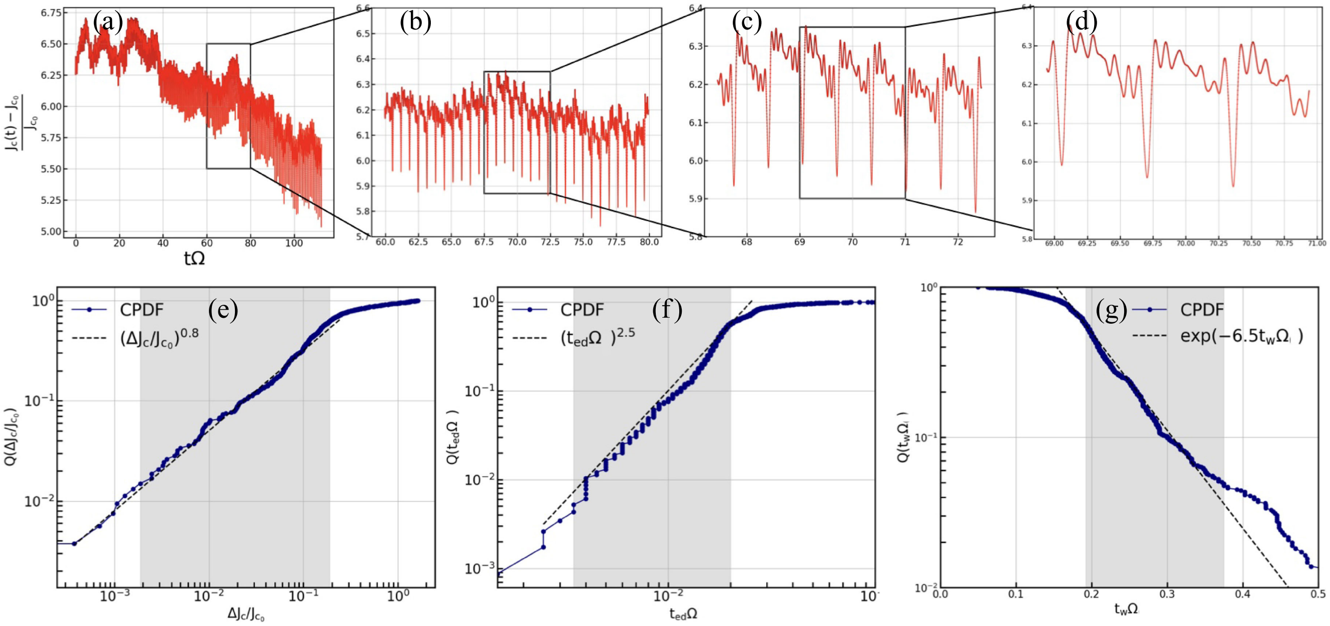

FIG. 13. (a) Time series of the crust angular momentum $(\mathrm{J}_c - \mathrm{J}_{c_0})/\mathrm{J}_{c_0}$. (b)–(d) are the zoomed versions of the rectangular regions shown in the preceding plots. Log-Log plots of (e) the CPDF $\mathrm{Q}(\Delta\mathrm{J}_c/\mathrm{J}_{c_0})$ of the event size and (f) the CPDF $\mathrm{Q}(t_{\mathrm{ed}}\Omega)$ of the event duration. (g) Semilog plot of the CPDF $\mathrm{Q}(t_w\Omega)$ of the waiting time. J_{c_0} and Ω are the initial angular momentum and initial angular velocity of the crust, respectively.

been observed for certain pulsars [e.g., PSR J 1825-0935 has glitch-size-PDF exponent $\simeq 0.36$] [30]. In Ref. [3], it has been noted that range of glitching sizes depends on Ω. In addition, we find that these sizes also depend on B_{ext}.

We have noted above that Poisson-equation-induced interaction between the neutron superfluid and the proton superconductor makes superfluid vortices approach superconductor flux tubes. As the crust decelerates, the neutron vortices leave the condensate abruptly. The associated jumps in $\mathrm{J}_c(t)$ are somewhat sharper in time but smaller in amplitude than those in the GPPE model of Ref. [3]. Consequently, our values of the exponents β and γ are about 10% larger than those in Ref. [3], but still comfortably in the observational range [30] $-0.13 \lesssim -(\beta - 1) \lesssim 2.4$. The inclusion of current-current and density-density interactions [Eq. (4)] may reduce the sizes of glitches, by slowing down the ejection of vortices from the condensate. Furthermore, we expect that the current-entrainment term in Eq. (21), which induces a magnetic field inside neutron vortices, could reduce glitch sizes.

V. CONCLUSIONS

We have developed a theoretical framework for studying the coupled motion of neutron-superfluid vortices and proton-flux tubes in a gravitationally collapsed condensate. In this framework we have employed (a) a 3D GPPE for neutron Cooper pairs, (b) the RTGLE for proton Cooper pairs, (c) the Maxwell equation for the vector potential $\mathbf{A}$, and (d) Newtonian gravity and interactions, both direct and induced by the Poisson equation, between the neutron and proton subsystems. For a pulsar we have included, in addition, a crust potential as in Ref. [3]. The recent studies in Refs. [24,25,68] use the Gross-Pitaevskii-Equation and Ginzburg-Landau equation (imaginary time) together with a *static ansatz* for $\mathbf{A}$ in a *harmonic trap*. We have gone well beyond these earlier studies by including Newtonian gravity in the GPPE and RTGLE together with *the complete Maxwell equations* for $\mathbf{A}$. To the best of our knowledge, this has not been attempted hitherto in the context of pulsars.

Our imaginary-time studies of the GPPE (19) and the RTGLE (20) reveals that, even in the absence of any direct interaction ($\gamma = 0$), the neutron-superfluid vortices and proton-superconductor flux tubes interact gravitationally through the Poisson equation (21). By including the Maxwell equations, we demonstrate, for the first time, that neutron-superfluid vortices display an induced magnetization whose magnitude is proportional to $\frac{\gamma q}{c^2 \epsilon_0} \mathbf{J}_n |\psi_p|^2$. This magnetization plays a crucial role in the expulsion of vortices from the pulsar. The angle Θ is an important control parameter in our model. For example, if $\Theta = 30°$, proton flux tubes gradually endeavor to align themselves with the rotation axis over time [Figs. 8(a)–8(c)], but they also exhibit a tendency to adhere to the external magnetic field; this competition leads to frustration in the proton-superconductor flux tubes, which are no longer straight but become distorted [Figs. 8(b) and 8(h)].

The real-time dynamics of the GPPE (19), RTGLE (20), and the Maxwell equations (21) can be applied qualitatively to pulsars. We must, of course, incorporate a pulsar-crust potential V_θ, described, at the simplest level, by the polar angle θ in Eq. (14). This provides a minimal model for studying pulsar glitches. Our investigation reveals that the proton-superconductor flux tubes remain anchored to the crust by the external magnetic field $\mathbf{B}_{\text{ext}}$, while neutron-superfluid vortices leave the condensate and give rise to the glitching phenomenon, the complicated time evolution of the crust angular momentum $\mathrm{J}_c(t)$, which displays signatures of SOC. Although pulsar glitches have been obtained recently in the GPPE model [3], they have not been studied in the presence of proton-superconductor flux tubes, whose dynamics affects pulsar glitches and the time series of $\mathrm{J}_c(t)$ significantly [as we can see by comparing Fig. 13 with Fig. 4(b) in Ref. [3]].

The SOC that we obtain in our model for pulsars, which generalizes the earlier work from our group [3], is akin to what has been obtained in some pulsars; e.g., in the pulsar PSR J 1825-0935, the glitch-size exponent $\beta \simeq 0.36$. Given the simplicity of our model, this is indeed gratifying. It is important to note that neutrons in the outer core of a neutron star are strongly interacting and are sometimes argued to scatter through p-wave interactions [16]. However, the Gross-Pitaevskii (GP) model of neutron Cooper pairs is applicable for weakly interacting neutrons and considers only s-wave interactions. Our interest lies in the dynamics of neutron vortices, which can be modeled using the s-wave interacting GP equation. This approach has previously been applied in modeling the outer core of neutron stars [24,25,68]. In our simulations, some ratios match closely the values found in typical pulsars; in the outer core of a neutron star, the proton to neutron number density ratio is $\frac{n_p}{n_n} \simeq 0.05$; we consider the range $0.5 \le \frac{n_p}{n_n} \le 1$. Furthermore, we choose the ratio of the neutron and proton coherence lengths $\frac{\xi_n}{\xi_p} = 2$, which agrees with the value found in neutron stars [69]. The London parameter κ for type II superconducting proton Copper pairs is chosen to be greater than $\frac{1}{\sqrt{2}}$, so that we have an Abrikosov phase. However, it is important to note that numerical studies cannot achieve spatial and temporal scales and resolutions that are in the ranges of direct relevance to pulsars. In particular, the radius of a typical neutron star is $\simeq 10$ km; by contrast, the core sizes of neutron-superfluid vortices are $\simeq 10^{-15}$ m; the ratio of the speed of light to that of sound $\frac{c}{c_s} \simeq 10^6$, which is a challenge for any simulation. The number of neutron-superfluid vortices that thread a pulsar is estimated to be $N_v = 10^{16}$; this is far in excess of what can be simulated on even the world's biggest computers. The number of vortices in our model is given as $N_v = \frac{L}{2} \sqrt{\frac{\beta}{\alpha}}$, where $L = 2\pi$

is the length of the simulation box and α and β are given in Table I. For the values we use in our simulations, namely, $\alpha = 0.2$ and $\beta = 5$, we have $N_v \sim 15$–20 vortices. We can increase N_v by increasing either the size of our simulation or the ratio β/α (or both); but these are limited severely by computational facilities.

ACKNOWLEDGMENTS

We thank the Indo-French Centre for Applied Mathematics (IFCAM), the Science and Engineering Research Board (SERB), and the National Supercomputing Mission (NSM), India for support, and the Supercomputer Education and Research Centre (IISc) for computational resources.

APPENDIX

The total angular momentum of the system is $\mathrm{J} = \mathrm{J}_z + \mathrm{J}_c$, with J_c, the crust angular momentum, and J_z, the angular momentum of the system without the crust, which are, respectively,

$$\mathrm{J}_c = I_c \frac{d\theta}{dt} \quad \text{and}$$

$$\mathrm{J}_z = \int d^3\mathbf{x}\psi_n^*(\hat{\mathbf{e}}_z \times \mathbf{r}) \cdot (-i\hbar\nabla)\psi_n + \int d^3\mathbf{x}\psi_p^*(\hat{\mathbf{e}}_z \times \mathbf{r}) \cdot (-i\hbar\nabla)\psi_p, \tag{A1}$$

where I_c is the moment of inertia of the crust. In the absence of friction [$\alpha = 0$ in Eq. (14)], the total angular momentum is conserved in an infinite system. In the spatially periodic cubical domain that we consider, this conservation is only approximate because this domain does not have strict rotational invariance (see Ref. [3] for a detailed discussion).

---

[1] A. K. Verma, R. Pandit, and M. E. Brachet, Formation of compact objects at finite temperatures in a dark-matter-candidate self-gravitating bosonic system, Phys. Rev. Res. **3**, L022016 (2021).

[2] S. Shukla, A. K. Verma, M. E. Brachet, and R. Pandit, Gravity- and temperature-driven phase transitions in a model for collapsed axionic condensates, Phys. Rev. D **109**, 063009 (2024).

[3] A. K. Verma, R. Pandit, and M. E. Brachet, Rotating self-gravitating Bose-Einstein condensates with a crust: A model for pulsar glitches, Phys. Rev. Res. **4**, 013026 (2022).

[4] V. Radhakrishnan and R. N. Manchester, Detection of a change of state in the pulsar PSR 0833-45, Nature (London) **222**, 228 (1969).

[5] P. E. Boynton, E. J. Groth III, R. B. Partridge, and D. T. Wilkinson, Precision measurement of the frequency decay of the crab nebula pulsar, NP 0532, Astrophys. J. **157**, L197 (1969).

[6] R. N. Manchester, Pulsar glitches, Proc. Int. Astron. Union **13**, 197 (2017).

[7] G. Baym, C. Pethick, and D. Pines, Superfluidity in neutron stars, Nature (London) **224**, 673 (1969).

[8] A. Migdal, Superfluidity and the moments of inertia of nuclei, Nucl. Phys. **13**, 655 (1959).

[9] N. Chamel and P. Haensel, Physics of neutron star crusts, Living Rev. Relativity **11**, 10 (2008).

[10] B. Haskell and A. Melatos, Models of pulsar glitches, Int. J. Mod. Phys. D **24**, 1530008 (2015).

[11] A. Basu, P. Char, R. Nandi, B. C. Joshi, and D. Bandyopadhyay, Glitch behavior of pulsars and contribution from neutron star crust, Astrophys. J. **866**, 94 (2018).

[12] G. Mendell, Superfluid hydrodynamics in rotating neutron stars. I. Nondissipative equations, Astrophys. J. **380**, 515 (1991).

[13] V. Graber, N. Andersson, K. Glampedakis, and S. K. Lander, Magnetic field evolution in superconducting neutron stars, Mon. Not. R. Astron. Soc. **453**, 671 (2015).

[14] V. Ginzburg and D. Kirzhnits, On the superconductivity of electrons at the surface levels, Zh. Eksp. Teor. Fiz. **46**, 397 (1964), http://jetp.ras.ru/cgi-bin/e/index/e/19/1/p269?a=list.

[15] R. A. Wolf, Some effects of the strong interactions on the properties of neutron-star matter, Astrophys. J. **145**, 834 (1966).

[16] B. Haskell and A. Sedrakian, Superfluidity and superconductivity in neutron stars, in *The Physics and Astrophysics of Neutron Stars*, edited by L. Rezzolla, P. Pizzochero, D. I. Jones, N. Rea, and I. Vidaña (Springer International Publishing, Cham, 2018), pp. 401–454.

[17] V. Khomenko and B. Haskell, Modelling pulsar glitches: The hydrodynamics of superfluid vortex avalanches in neutron stars, Publ. Astron. Soc. Aust. **35**, e020 (2018).

[18] G. Howitt and A. Melatos, Antiglitches in accreting pulsars from superfluid vortex avalanches, Mon. Not. R. Astron. Soc. **514**, 863 (2022).

[19] G. Watanabe and C. J. Pethick, Superfluid density of neutrons in the inner crust of neutron stars: New life for pulsar glitch models, Phys. Rev. Lett. **119**, 062701 (2017).

[20] E. Poli, T. Bland, S. J. M. White, M. J. Mark, F. Ferlaino, S. Trabucco, and M. Mannarelli, Glitches in rotating supersolids, Phys. Rev. Lett. **131**, 223401 (2023).

[21] L. Warszawski and A. Melatos, Gross–Pitaevskii model of pulsar glitches, Mon. Not. R. Astron. Soc. **415**, 1611 (2011).

[22] L. Warszawski, A. Melatos, and N. G. Berloff, Unpinning triggers for superfluid vortex avalanches, Phys. Rev. B **85**, 104503 (2012).

[23] J. A. Sauls, Superfluidity in the interiors of neutron stars, in *Timing Neutron Stars*, edited by H. Ögelman and E. P. J. van den Heuvel (Springer Netherlands, Dordrecht, 1989), pp. 457–490.

[24] L. V. Drummond and A. Melatos, Stability of interlinked neutron vortex and proton flux tube arrays in a neutron star: Equilibrium configurations, Mon. Not. R. Astron. Soc. **472**, 4851 (2017).

[25] L. V. Drummond and A. Melatos, Stability of interlinked neutron vortex and proton flux-tube arrays in a neutron star —II. Far-from-equilibrium dynamics, Mon. Not. R. Astron. Soc. **475**, 910 (2017).

[26] A. A. Verheijen, J. M. van Ruitenbeek, R. de Bruyn Ouboter, and L. J. de Jongh, Measurement of the London moment in two high-temperature superconductors, Nature (London) **345**, 418 (1990).

[27] P. Bak, C. Tang, and K. Wiesenfeld, Self-organized criticality: An explanation of the 1/f noise, Phys. Rev. Lett. **59**, 381 (1987).

[28] H. J. Jensen, Frontmatter, in *Self-Organized Criticality: Emergent Complex Behavior in Physical and Biological Systems*, Cambridge Lecture Notes in Physics (Cambridge University Press, Cambridge, England, 1998), pp. i–vi.

[29] D. L. Turcotte, Self-organized criticality, Rep. Prog. Phys. **62**, 1377 (1999).

[30] A. Melatos, C. Peralta, and J. S. B. Wyithe, Avalanche dynamics of radio pulsar glitches, Astrophys. J. **672**, 1103 (2008).

[31] *The Physics and Astrophysics of Neutron Stars*, edited by L. Rezzolla, P. Pizzochero, D. I. Jones, N. Rea, and I. Vidaña (Springer, New York, 2018), Vol. 457.

[32] J. M. Lattimer and M. Prakash, The physics of neutron stars, Science **304**, 536 (2004).

[33] E. Gibney, Neutron stars set to open their heavy hearts, Nature (London) **546**, 18 (2017).

[34] B. P. Kosyakov, Lagrangian formalism in electrodynamics, in *Introduction to the Classical Theory of Particles and Fields* (Springer Berlin Heidelberg, Berlin, Heidelberg, 2007), pp. 195–248.

[35] C. A. Van Eysden, *Superfluid Spin Up and Pulsar Glitch Recovery* (University of Melbourne, School of Physics, Melbourne, 2011).

[36] D. Bhattacharya and G. Srinivasan, The evolution of neutron star magnetic fields, in *Neutron Stars: Theory and Observation*, edited by J. Ventura and D. Pines (Springer Netherlands, Dordrecht, 1991), pp. 219–233.

[37] P.-H. Chavanis, Mass-radius relation of newtonian self-gravitating Bose-Einstein condensates with short-range interactions. I. Analytical results, Phys. Rev. D **84**, 043531 (2011).

[38] P.-H. Chavanis, Collapse of a self-gravitating Bose-Einstein condensate with attractive self-interaction, Phys. Rev. D **94**, 083007 (2016).

[39] P.-H. Chavanis, Phase transitions between dilute and dense axion stars, Phys. Rev. D **98**, 023009 (2018).

[40] E. Cotner, Collisional interactions between self-interacting nonrelativistic boson stars: Effective potential analysis and numerical simulations, Phys. Rev. D **94**, 063503 (2016).

[41] A. Bernal and F. S. Guzmán, Scalar field dark matter: Head-on interaction between two structures, Phys. Rev. D **74**, 103002 (2006).

[42] E. J. M. Madarassy and V. T. Toth, Evolution and dynamical properties of Bose-Einstein condensate dark matter stars, Phys. Rev. D **91**, 044041 (2015).

[43] M. Tinkham, *Introduction to Superconductivity*, 2nd ed. (Dover Publications, New York, 2004).

[44] M. Falco, S. H. Hansen, R. Wojtak, and G. A. Mamon, Why does the Jeans Swindle work?, Mon. Not. R. Astron. Soc. **431**, L6 (2013).

[45] M. K.-H. Kiessling, The, "jeans swindle": A true story–mathematically speaking, Adv. Appl. Math. **31**, 132 (2003).

[46] P. J. E. Peebles, *The Large-Scale Structure of the Universe* (Princeton University Press, Princeton, 1980).

[47] A. A. Abrikosov, Nobel lecture: Type-II superconductors and the vortex lattice, Rev. Mod. Phys. **76**, 975 (2004).

[48] D. Hipkins, W. Felson, and Y. M. Xiao, Measurement of the London moment, Czech. J. Phys. **46**, 2871 (1996).

[49] E. Babaev and B. Svistunov, Rotational response of superconductors: Magnetorotational isomorphism and rotation-induced vortex lattice, Phys. Rev. B **89**, 104501 (2014).

[50] G. Krstulovic and M. Brachet, Energy cascade with small-scale thermalization, counterflow metastability, and anomalous velocity of vortex rings in Fourier-truncated Gross-Pitaevskii equation, Phys. Rev. E **83**, 066311 (2011).

[51] T. Y. Hou and R. Li, Computing nearly singular solutions using pseudo-spectral methods, J. Comput. Phys. **226**, 379 (2007).

[52] R. Kato, Y. Enomoto, and S. Maekawa, Computer simulations of dynamics of flux lines in type-II superconductors, Phys. Rev. B **44**, 6916 (1991).

[53] E. Babaev and N. W. Ashcroft, Violation of the London law and Onsager–Feynman quantization in multicomponent superconductors, Nat. Phys. **3**, 530 (2007).

[54] This is in contrast to the behavior of the Abrikosov lattice, for a non-rotating superconductor in an external magnetic field [49].

[55] P. K. Mishra, J. Herault, S. Fauve, and M. K. Verma, Dynamics of reversals and condensates in two-dimensional Kolmogorov flows, Phys. Rev. E **91**, 053005 (2015).

[56] V. Shukla, S. Fauve, and M. Brachet, Statistical theory of reversals in two-dimensional confined turbulent flows, Phys. Rev. E **94**, 061101 (2016).

[57] M. Berhanu, R. Monchaux, S. Fauve, N. Mordant, F. Pétrélis, A. Chiffaudel, F. Daviaud, B. Dubrulle, L. Marié, F. Ravelet *et al.*, Magnetic field reversals in an experimental turbulent dynamo, Europhys. Lett. **77**, 59001 (2007).

[58] F. Pétrélis and S. Fauve, Chaotic dynamics of the magnetic field generated by dynamo action in a turbulent flow, J. Phys. Condens. Matter **20**, 494203 (2008).

[59] C. Gissinger, E. Dormy, and S. Fauve, Morphology of field reversals in turbulent dynamos, Europhys. Lett. **90**, 49001 (2010).

[60] J.-P. Valet and A. Fournier, Deciphering records of geomagnetic reversals, Rev. Geophys. **54**, 410 (2016).

[61] C. Laj, Geomagnetic field, polarity reversals, in *Encyclopedia of Solid Earth Geophysics* (Springer, New York, 2021), pp. 507–514.

[62] T. Alberti, F. Florindo, P. De Michelis, and G. Consolini, Unveiling geomagnetic reversals: Insights from tipping points theory, Geophys. Res. Lett. **50**, e2023GL105646 (2023).

[63] C. Dobbs, D. Price, A. R. Pettitt, M. R. Bate, and T. Tricco, Magnetic field evolution and reversals in spiral galaxies, Mon. Not. R. Astron. Soc. **461**, 4482 (2016).

[64] J. Han, R. Manchester, W. van Straten, and P. Demorest, Pulsar rotation measures and large-scale magnetic field reversals in the galactic disk, Astrophys. J. Suppl. Ser. **234**, 11 (2018).

[65] P. Charbonneau, Solar dynamo theory, Annu. Rev. Astron. Astrophys. **52**, 251 (2014).

[66] I. F. Malov and E. B. Nikitina, Angles between the rotational axis and magnetic moment in 80 pulsars from observations near 1 GHz, Astronomy Reports **55**, 19 (2011).

[67] P. Reichley and G. Downs, Observed decrease in the periods of pulsar PSR 0833–45, Nature (London) **222**, 229 (1969).

[68] K. H. Thong, A. Melatos, and L. V. Drummond, Stability of interlinked neutron vortex and proton flux-tube arrays in a neutron star—III. Proton feedback, Mon. Not. R. Astron. Soc. **521**, 5724 (2023).

[69] T. S. Wood and V. Graber, Superconducting phases in neutron star cores, Universe **8**, 228 (2022).